Ore Geology Reviews 57 (2014) 560–573

Contents lists available at ScienceDirect

Ore Geology Reviews

journal homepage: www.elsevier.com/locate/oregeorev

Postdated melting of subcontinental lithospheric mantle by the Emeishan mantle plume: Evidence from the Anyi intrusion, Yunnan, SW China

Song-Yue Yu, Xie-Yan Song *, Lie-Meng Chen, Xiao-Biao Li

State Key Laboratory of Ore Deposit Geochemistry, Institute of Geochemistry, Chinese Academy of Sciences, 46 Guanshui Road, Guiyang 550002, China

ARTICLE INFO

Article history:
Received 28 April 2013
Received in revised form 5 August 2013
Accepted 8 August 2013
Available online 19 August 2013

Keywords:
Emeishan large igneous province
Fe–Ti oxide
Lithospheric mantle
Garnet pyroxenite

ABSTRACT

The Anyi intrusion is located in the central zone of Emeishan large igneous province (ELIP), SW China. It outcrops in an area of about 0.65 km^2 and ~1 km thick and dips to the southwest. The Anyi intrusion consists of a lower clinopyroxenite zone, middle gabbro zone, and an upper monzonite–syenite zone. Up to 400 m thick stratiform disseminated Fe–Ti oxide layer with grades of 16–18 wt.% total Fe is hosted in the lower clinopyroxenite zone. Zircon SHRIMP U–Pb age (247 ± 3 Ma) indicates that the Anyi intrusion represents postdated mafic magmatism resulting from the ~260 Ma Emeishan mantle plume. Compared with the typical oxide-bearing intrusions (such as Panzhihua and Baima) formed at ~260 Ma in the ELIP, the Anyi intrusion is characterized by high alkaline contents and LREE/HREE ratios, extremely low εNd values (−6.2 to −7.6) and moderate high $(^{87}Sr/^{86}Sr)_i$ values (0.7072 to 0.7086). These characteristics of the Anyi intrusion cannot be explained by fractional crystallization or crustal contamination, but may reflect a unique enriched continental lithospheric mantle source (a mantle source mixed between garnet pyroxenite and spinel peridotite). We propose that the postdated mafic magmatism associated with the formation of the Anyi intrusion and its Fe–Ti oxide ore may be the product of melting of a mantle source mixed between garnet pyroxenite and spinel peridotite in the shallow lithosphere caused by conductive heating combined with lithosphere thinning due to plume–lithosphere interaction.

1. Introduction

Although the most extensive tholeiitic magmatism (more than 80% of the total volume) derived from mantle plume commonly occurred within 1 Myr, weakly eruptive and intrusive processes may be continued or postponed 10–30 Myrs following the main plume impact (Courtillot and Renne, 2003; Karlstrom and Richards, 2011; Richards et al., 1989). For example, multistage magmatism continues from 62 Ma to 52 Ma in the North Atlantic Large Igneous Province (LIP) (Jerram and Widdowson, 2005; Saunders et al., 1997). Similarly, both Paraná–Etendeka and Columbia River flood basalt eruptions occurred over a long time interval (~12 Ma) (Gibson et al. 2006; Hooper, 1997). Although a lot of investigations have been carried out on the main stage of mantle plume tholeiitic magmatism, studies focused on the postdated mantle-derived magmatism are still rare. Whether or not the postponed mantle-derived magmatism is genetically associated with the plume activity, what is nature of the mantle source and how the mantle partially melts have not been well addressed.

The Permian Emeishan large igneous province (ELIP) in southwest China consists of voluminous continental flood basalts covering an area more than 5×10^5 km^2 and a large number of genetically related mafic–ultramafic and felsic intrusions (Song et al., 2001; Xiao et al., 2003; Xu et al., 2001). It is generally accepted that the main pulse of the mafic and felsic magmatism of the ELIP occurred at ~260 Ma (Chung and Jahn, 1995; He et al., 2007; Zhou et al., 2002a). However, the Cida intrusive complex and Baima mafic dykes in the central ELIP have been dated at ~242–243 Ma (Luo et al., 2013; Shellnutt and Zhou, 2008) (Fig. 1). The rhyolitic tuff containing ~238 Ma zircons at the tops of the Emeishan basalt sequence and ~251 Ma I-type granites from Ailanghe, which were considered to be resulting from partial lower crust melting due to underplating of mafic magmas, have been discovered in the central ELIP as well (Xu et al., 2008, 2010; Zhong et al., 2007). Why the delayed mafic magmas after the peak magmatism of the ELIP occurred and what the nature of the mantle source is are still not understood.

Most of the layered intrusions hosting huge Fe–Ti oxide ore deposits (such as Panzhihua, Baima, Hongge) in the central ELIP have been dated at ~260 ± 3 Ma (Shellnutt et al., 2009; Zhong and Zhu, 2006; Zhou et al., 2005, 2008). However, the new zircon U–Pb ages obtained in this study indicate that the Fe–Ti oxide mineralized Anyi intrusion was emplaced at ~247 ± 3 Ma. Combined petrological, elemental and Sr–Nd isotopic data of the Anyi intrusion permit us to propose that the associated magma may be derived from melting of a mantle source mixed between garnet pyroxenite and spinel peridotite in the shallow lithosphere caused by conductive heating combined with lithosphere thinning during plume–lithosphere interaction.

* Corresponding author. Tel.: +86 851 5895538; fax: +86 851 5891664.
E-mail address: songxieyan@vip.gyig.ac.cn (X.-Y. Song).

0169-1368/$ – see front matter © 2013 Elsevier B.V. All rights reserved.
http://dx.doi.org/10.1016/j.oregeorev.2013.08.006

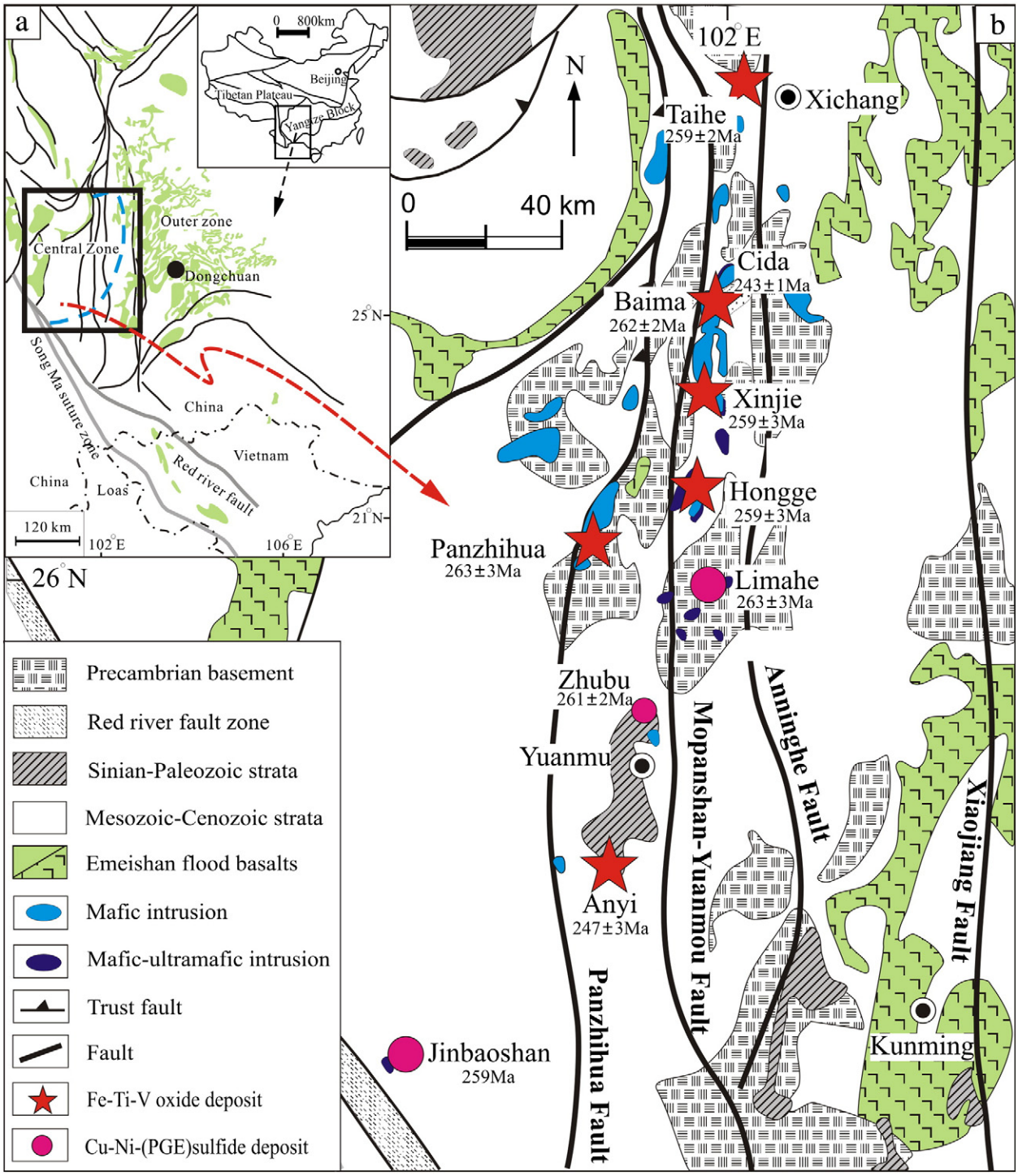

Fig. 1. (a) Distribution the Emeishan flood basalts. (b) Regional geological map of the central zone of the Emeishan large igneous province and locations of the mafic–ultramafic intrusions associated with Cu–Ni–(PGE) sulfide deposits and Fe–Ti–V oxide deposits (modified from Song et al., 2009). The ages of mafic–ultramafic intrusions are from Zhou et al., 2005, 2008; Tao et al., 2007; Zhong et al., 2011; Luo et al., 2013.

2. Regional geological setting

Southwest China comprises the Yangtze Block in the east and the Tibetan Plateau in the west (Fig. 1). Neoproterozoic arc plutonic-metamorphic assemblages occur along the western and northern margins of the Yangtze Block, which are believed to have been related to the subduction of Rodinian oceanic lithosphere toward the Yangtze Block during a period from 860 to 760 Ma (Zhou et al., 2002b). Since the early Permian, thick carbonate sequences began to deposit as a response to extensive transgression and basin subsidence (Sichuan, 1991; Yunnan, 1990). The Late Permian Emeishan flood basalts unconformably overlay the early Late Permian limestones and in turn are overlain by Late Permian to Triassic and Cretaceous terrestrial sandstones and conglomerates (Sichuan, 1991; Yunnan, 1990).

The ELIP was divided into a central zone and an outer zone (Fig. 1, Chung and Jahn, 1995; Song et al., 2003, 2005; Xu et al., 2001), and the thickness of the Emeishan flood basalts range from more than 2000 m in the central zone to several hundred meters in the outer zone (Song et al., 2008a; Xu et al., 2004). The central zone of the ELIP is characterized by low-Ti basalts overlain by high-Ti basalts,

whereas the outer zone consists dominantly of high-Ti basalts. In addition, large layered intrusions and A- and I-type syenite and granite plutons are exposed in the central zone of the ELIP (Zhong et al., 2002, 2003). A few of Ni–Cu–(PGE) deposits are hosted in the small mafic–ultramafic intrusions, such as Limahe, Jinbaoshan and Zhubu deposits (Song et al., 2008b; Tao et al., 2007, 2008). Several giant Fe–Ti–V oxide deposits are hosted in the large layered intrusions, such as Panzhihua, Baima, Hongge, Xinjie and Taihe deposits in the central zone (Fig. 1) (Bai et al., 2012; Song et al., 2013; Zhang et al., 2012; Zhong et al., 2002, 2003, 2004; Zhou et al., 2005).

3. Petrography of the Anyi intrusion

The Anyi intrusion is located between the Panzhihua fault and Mopanshan–Yuanmou fault in the central zone of the ELIP, about 130 km south of Panzhihua (Fig. 1). It outcrops an area of about 0.65 km^2 and intrudes into the Proterozoic carbon-rich talc slate (Fig. 2). The upper portion of the intrusion has been eroded and is unconformably covered by the Cretaceous mudstone and sandstone.

The Anyi intrusion can be divided into the Lower clinopyroxenite zone, Middle gabrro zone, and Upper monzonite–syenite zone according to cumulus mineral assemblage (Fig. 2). The Lower zone is 800–-1100 m thick and consists of olivine clinopyroxenite, clinopyroxenite, and magnetite clinopyroxenite (disseminated oxide ore) from the base upwards. The medium- to coarse-grained olivine clinopyroxenite consists of ~10–25% olivine, ~65–75% clinopyroxene and ~5–10% magnetite. When olivine content decreases to less than 5%, it is named as clinopyroxenite, which also contains ~5% biotite and minor plagioclase. The coarse-grained magnetite clinopyroxenite (disseminated Fe–Ti oxide ore) is 300–400 m thick and typically consists of ~15–25% magnetite, ~50–60% clinopyroxene, ~5–10% biotite, and minor ilmenite, plagioclase and apatite (Fig. 3a). Exsolution of ilmenite lamellae in the magnetite is very common in the magnetite clinopyroxenites (Fig. 3b). 10 million tonnes disseminated Fe–Ti oxide ores with average grades of ~30 wt.% Fe_2O_3, ~7.0 wt.% TiO_2, ~0.2 wt.%V_2O_5, and 0.2–0.5 ppm (Pt + Pd) are hosted in the upper part of the Lower zone (Panxi Geological Unit, 1984).

The Middle zone is up to 150 m thick and consists of dominantly medium- to coarse-grained monzogabbro, which commonly contains ~50–60% clinopyroxene, ~5–10% orthoclase, ~15–25% plagioclase, ~10–15% magnetite, ~5–10% biotite, ~2–5% apatite and minor hornblende occurring as reaction rims of clinopyroxene grains. The boundary between the Lower clinopyroxenite zone and the Middle gabrro zone has been defined by remarkable increase of feldspar and decreases of clinopyroxene and magnetite (Fig. 3c).

The Upper zone is more than 160 m thick and consists of monzonite and overlying syenite. The monzonite typically contains ~30–40% clinopyroxene, ~15–30% orthoclase, ~20–25% plagioclase, ~5–10% hornblende, and ~5–10% Fe–Ti oxides, and minor biotite and apatite. The syenite consists of ~20–30% clinopyroxene, ~45–50% orthoclase, ~15–20% plagioclase, ~5–10% hornblende. The boundary between the Middle zone monzogabbro and Upper zone monzonite has been defined by remarkable increase of feldspar and hornblende and decrease of clinopyroxene (Fig. 3d). Hornblende is most abundant in the Upper zone and poikilitically enclosing clinopyroxene and apatite grains. The gradational boundaries between the three lithologic zones indicate a fractional crystallization sequence. Rock textures suggest that the sequence of mineral crystallization in the Anyi intrusion is olivine → clinopyroxene → Fe–Ti oxides → feldspar → apatite → biotite + hornblende.

4. Sampling and analytical methods

Samples of the Anyi intrusion were collected from a north–south surface traverse across the lower magnetite clinopyroxenite unit, middle gabbro zone and upper monzonite unit (Fig. 2a). Zircons were separated from a monzonite sample (AY-62) (>30 kg) using conventional heavy liquid and magnetic techniques. Representative zircon grains were hand-picked under binocular microscope and mounted in an epoxy resin disk, and then polished and coated with a gold film. Zircons were investigated with transmitted and reflected light as well as cathodoluminescence (CL) to reveal their external and internal structures. The U–Pb isotopic analyses were performed using the Sensitive High-Resolution Ion Microprobe (SHRIMP-II) at the Chinese Academy of Geological Sciences (Beijing) (Table 1). Procedures are described in detail by Compston et al. (1992) and Williams (1998). The U–Pb isotope data was collected after five scans and a reference zircon TEM (417 Ma) (Black et al., 2003) was analyzed after every four spots. The uncertainties in ages are cited as 1σ, and the weighted mean ages are quoted at the 95% confidence level (2σ). The U–Pb isotope data was treated

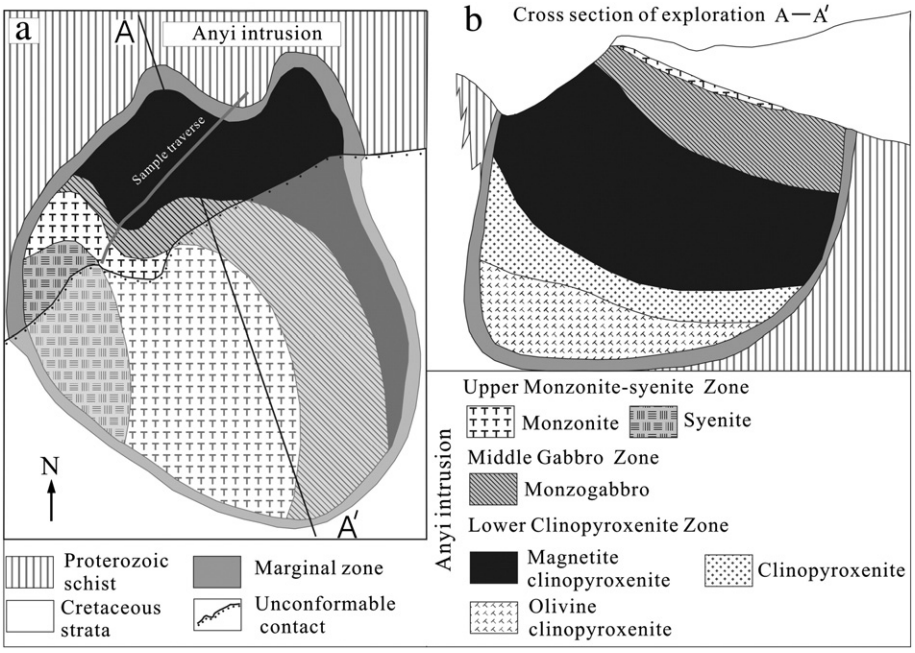

Fig. 2. (a) Simplified geological map of the Anyi intrusion. Sample traverse is also shown. (b) Cross section of exploration A–A′ from the Anyi intrusion (after Panxi Geological Unit, 1984).

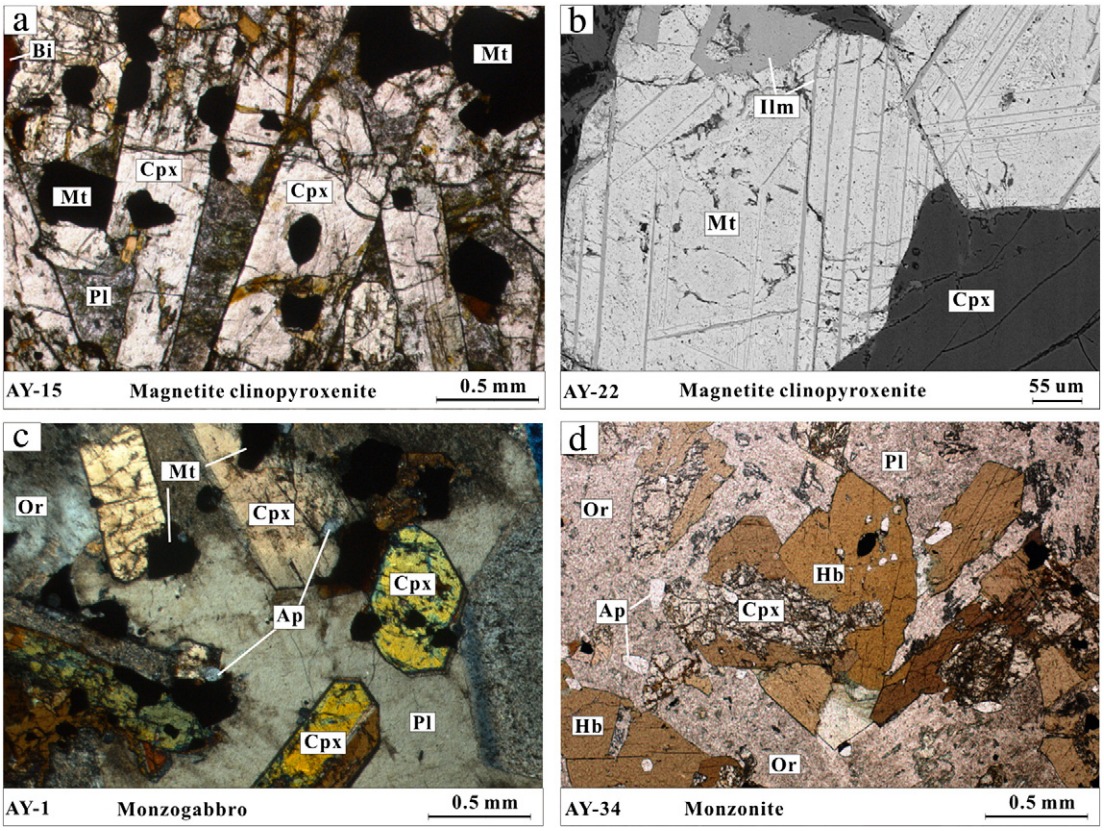

Fig. 3. Texture photos of the Anyi rocks under microscope. (a) Interstitial plagioclase (Pl) and biotite (Bi) between cumulus clinopyroxene (cpx) and magnetite (Mt) in the magnetite clinopyroxenite. Sub-rounded magnetite is enclosed by large tabular clinopyroxene, under plane-polarized light; (b) exsolution of ilmenite (Ilm) lamellae and small grains from the host magnetite, BSE image; (c) enhedral clinopyroxene with median grain size, interstitial magnetite and apatite surrounded by a large plagioclase crystal, under cross-polarized light; (d) clinopyroxene is replaced by hornblende (Hb), enhedral apatite is enclosed by hornblende or orthoclase (Or), under plane-polarized light.

following Compston et al. (1992) with the ISOPLOT program of Ludwig (2001).

Samples in this study were cut to remove weathering rinds. Relatively fresh interiors were used for bulk-rock analyses. The rocks were crushed in a steel mortar and ground in a steel mill. Major oxides were analyzed with a PANalytical Axios-advance X-ray fluorescence spectrometer (XRF) at the Institute of Geochemistry, Chinese Academy of Science (IGCAS), using fused lithum–tetraborate glass pellets, and ferric and ferrous iron were determined by wet chemical method. The analytical precision is better than 5%. Loss on ignition (LOI) was obtained using 1 g powder heated up to 1100 °C for 1 h. Trace elements were analyzed using a Perkin-Elmer Sciex ELAN 6000 ICP-MS at the IGCAS. The powdered samples (50 mg) were dissolved in high-pressure Teflon bombs using a HF + HNO_3 mixture for 12 h at ca. 190 °C (Qi et al., 2000). Rh was used as an internal standard to monitor signal drift during counting. The international standard, GBPG-1 was used for analytical quality control. The analytical precision was generally better than 5% for all elements.

For Sr–Nd isotopic analyses, sample powders were spiked with mixed isotope tracers, and then dissolved in Teflon capsules with HF + HNO_3 acid. Sr and rare earth elements (REE) were separated on columns of Eichrom Co. Sr and REE resins using 0.1%HNO_3 as elutant. Nd was separated from the REE fractions on HDEHP columns using 0.18 N HCl as elutant. Isotopic measurements were performed via

Table 1
SHRIMP U–Pb isotopic data for zircons from the Anyi monzonites.

Sample/spot	$^{206}Pb_c$	U	Th	Th/U	$^{206}Pb^*$	$^{207}Pb^*/^{206}Pb^*$	$^{207}Pb^*/^{235}U$	$^{206}Pb^*/^{238}U$	$^{206}Pb^*/^{238}U$	$^{207}Pb^*/^{206}Pb^*$	$^{208}Pb^*/^{232}Th$
	(%)	(ppm)	(ppm)		(ppm)	±1σ%	±1σ%	±1σ%	Age ± 1σ (Ma)		
AY-62											
1.1	0.72	232	241	1.04	7.95	0.0506 ± 6.3	0.276 ± 6.7	0.0396 ± 2.1	250.2 ± 5.2	221 ± 150	240 ± 9
2.1	3.69	294	296	1.01	10.4	0.0490 ± 21	0.268 ± 22	0.0396 ± 2.3	250.3 ± 5.6	149 ± 500	263 ± 22
3.1	0.38	754	1299	1.72	24.5	0.0531 ± 2.4	0.276 ± 3	0.0377 ± 1.8	238.6 ± 4.2	331 ± 55	246 ± 5
4.1	0.41	224	245	1.09	7.82	0.0523 ± 5.8	0.292 ± 6.1	0.0404 ± 2.1	255.6 ± 5.1	300 ± 130	249 ± 9
5.1	0.00	152	119	0.78	5.11	0.0570 ± 4.0	0.307 ± 4.6	0.0390 ± 2.2	246.8 ± 5.3	492 ± 89	273 ± 11
6.1	0.75	218	233	1.07	7.19	0.0511 ± 5.0	0.268 ± 5.4	0.0381 ± 2.0	241.0 ± 4.8	246 ± 110	221 ± 8
7.1	0.00	99	81	0.82	1.93	0.0606 ± 6.4	0.189 ± 7.1	0.0227 ± 3.0	144.5 ± 4.3	624 ± 140	155 ± 9
8.1	0.71	236	239	1.01	8.31	0.0481 ± 4.4	0.271 ± 4.8	0.0408 ± 2.0	257.6 ± 5.1	106 ± 100	239 ± 8
9.1	0.28	219	149	0.68	7.46	0.0511 ± 4.6	0.279 ± 5	0.0396 ± 2.0	250.6 ± 5.0	245 ± 110	253 ± 10
10	0.00	179	204	1.14	5.85	0.0547 ± 3.7	0.287 ± 4.8	0.0380 ± 3.1	240.6 ± 7.2	400 ± 83	228 ± 9
11	0.50	220	281	1.28	7.35	0.0509 ± 4.7	0.271 ± 5.1	0.0386 ± 2.0	244.4 ± 4.9	236 ± 110	249 ± 8
12	22.24	86	101	1.17	1.69	0.0900 ± 65	0.220 ± 65	0.0177 ± 8.0	113.2 ± 9.0	1420 ± 1200	106 ± 49

(1) Errors are 1σ; Pbc and Pb* indicating the common and radiogenic portions, respectively. (2) Error in standard calibration was 0.69% (not included in above errors but required when comparing data from different mounts). (3) Common Pb corrected using measured ^{204}Pb.

thermal ionization mass spectrometry (TIMS) at the Institute of Geochemistry, Chinese Academy of Sciences. Mass fractionation corrections for Sr and Nd isotopic ratios were based on $^{86}Sr/^{88}Sr = 0.1194$ and $^{146}Nd/^{144}Nd = 0.7219$ respectively. The $^{87}Sr/^{86}Sr$ ratios of the NBS987 and NBS607 Sr isotopic standards and $^{143}Nd/^{144}Nd$ ratios of the BCR-1 and La Jolla Nd isotopic standards determined during this study are 0.710240 ± 15 (2σ), 1.20032 ± 30 (2σ), 0.512663 ± 9 (2σ) and 0.511862 ± 7 (2σ), respectively. Detailed sample preparation and analytical procedures followed Zhang et al. (2001).

5. Results

5.1. U–Pb zircon geochronology

Zircon crystals for age dating are separated from a monzonite sample (AY-62) of the Upper zone. The subhedral prismatic zircon grains are clear and show simple internal oscillatory zonation in CL images, an indication of magmatic origin. There is no evidence of overgrowths or inherited cores. The results of SHRIMP zircon U–Pb analysis are listed in Table 1. The zircons have highly variable abundances of Th (81–1299 ppm) and U (86–754 ppm), with Th/U ratios of 0.68–1.72. One zircon grain (Spot 7.1) gave a disconcordant $^{206}Pb/^{238}U$ age of 144.5 ± 4.3 Ma. Another zircon grain (Spot 12) with young $^{206}Pb/^{238}U$ age (113.2 ± 9.0 Ma) displays large error of $^{207}Pb/^{235}U$ (Table 1). The young $^{206}Pb/^{238}U$ ages of these two zircon grains are likely due to partial Pb loss or low radiogenic Pb concentrations ($^{206}Pb = 1.69$ and 1.93 ppm, respectively, Table 1). The remaining 10 analyses give a weighted mean $^{206}Pb/^{238}U$ age of 247 ± 3 Ma (Fig. 4).

5.2. Major and trace elements

Major element abundances are listed in Table 2 and illustrated in Fig. 5. Typical oxide-bearing intrusions in the ELIP, such as Panzhihua and Baima, are also shown for comparison. Consistent with the petrographic variation, the rocks of the Anyi intrusion exhibit variable chemical compositions. From the Lower zone magnetite clinopyroxenites to the Upper zone monzonites, contents of SiO_2 and Al_2O_3 increase from 36 to 49 wt.% and 4 to 15 wt.%, respectively, whereas contents of MgO and CaO decrease from 10 to 3.2 wt.% and 13 to 7.8 wt.%, respectively (Table 2). In the diagrams of SiO_2 versus TiO_2, Fe_2O_3 (Total) and MgO (Fig. 5a, b, d), the Anyi rocks plot in the domain shared by the Panzhihua and Baima intrusions, whereas in the diagrams of SiO_2 versus Al_2O_3 and K_2O (Fig. 5c, e), they plot out of the fields of the Panzhihua and Baima intrusions. In addition, the Anyi rocks display negative correlation between SiO_2 and CaO (Fig. 5f) in contrast to the positive correlation for the Panzhihua and Baima intrusions. Particularly, the Anyi rocks have contents of Zr and Nb significantly higher than the Panzhihua and Baima rocks at comparable SiO_2 contents (Fig. 5g–h). Additionally, the Anyi rocks show positive correlation between K_2O and Na_2O (Fig. 6a), relatively high P_2O_5 content (>0.6 wt.%) and extreme enrichment of rare earth element (REE) (Fig. 6b).

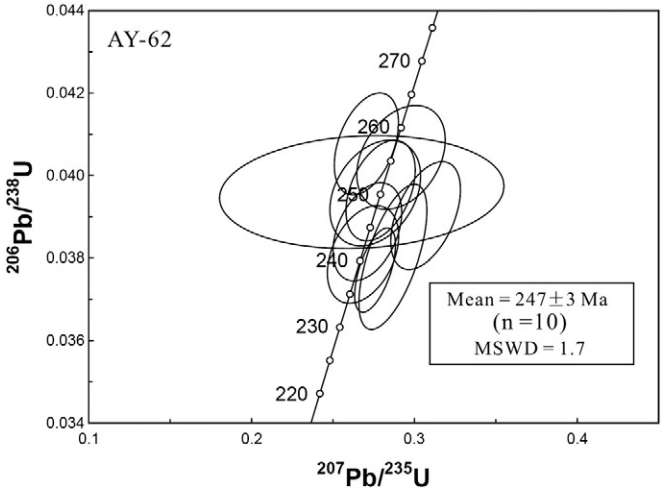

Fig. 4. SHRIMP zircon U–Pb concordia diagram of a monzonite (AY-62) from the Anyi intrusion, SW China.

In the chondrite normalized REE diagram, the Anyi magnetite clinopyroxenites have more significant enrichment in light REE and depletion in heavy REE than both the low-Ti and high-Ti Emeishan basalts (Fig. 7a). Additionally, they display significant negative Sr, P and K anomalies and positive Ti anomaly in the primitive mantle normalized trace element diagram, whereas the negative Nb, Ta and Zr anomalies are very weak (Fig. 7b). The abundances of REE and other incompatible elements of the Anyi monzogabbros and monzonites are significantly higher than those of the magnetite clinopyroxenites and display weaker Sr, P and K anomalies (Fig. 7c, d).

5.3. Sr–Nd isotope compositions

Rocks from the different zones of the Anyi intrusion display relatively homogeneous Sr–Nd isotopic values. Initial $^{86}Sr/^{87}Sr$ ratios of the Anyi rocks range from 0.7072 to 0.7086. εNd (t) values range from −6.2 to −7.6 (Table 3). In the diagram of εNd(t) versus $^{86}Sr/^{87}Sr(t)$ (Fig. 8), the Sr–Nd isotope compositions of the Panzhihua and Baima intrusions are similar to those of Emeishan high-Ti basalts, whereas the Limahe, Jinbaoshan and Zhubu mafic–ultramafic rocks, similar to the low-Ti basalts, display relatively low εNd (t) values and high initial $^{86}Sr/^{87}Sr$ ratios and define a crustal contamination trend. In contrast, most of the Anyi samples show very low εNd values and moderately high initial $^{86}Sr/^{87}Sr$ ratios, similar to those of Dongchuan tephrites.

6. Discussion

The young age (247 ± 3 Ma) indicates that the Anyi intrusion was formed more than 10 Ma later than the peak magmatism of the Emeishan mantle plume (~260 Ma) (He et al., 2007; Zhou et al., 2002a). As described above, compared with the ~260 Ma Panzhihua and Baima intrusions in the central ELIP, the Anyi intrusion is characterized by high concentrations of incompatible elements, high LREE/HREE ratios (La/Yb = 20.4–55.1), very low εNd (−6.2 to −7.6) and moderately high $(^{87}Sr/^{86}Sr)_i$ (0.7072 to 0.7086) (Figs. 7–8). These characteristics cannot be simply explained by fractional crystallization combined with crustal contamination, but reflect a unique mantle source. In the following discussion, we will mainly focus on the nature of the mantle source, and possible formation mechanisms of the delayed mafic magma.

6.1. Fractional crystallization and crustal contamination

The Anyi magnetite clinopyroxenites and monzogabbros have been variably altered after their emplacement. Secondary minerals, such as chlorite and albite, replace augite and plagioclase respectively. Loss on ignition (LOI) for most clinopyroxenites and monzogabbros ranges from 2.09 to 3.78 wt.%, whereas the monzonites were less altered with LOI ranging from 0.85 to 2.79 wt.% (Table 2). However, mobile elements of these rocks, such as Rb and Ba, show a roughly negative correlation with LOI (Fig. 9a–b). This implies only weak effect of the alteration on the trace element composition of the Anyi rocks. Even so, the following discussions will be mainly based on the immobile elements, such as REE, high field strength elements (HFSE), Th, Y and Ti to minimize the alteration effect.

The geochemical characteristics of the mafic and ultramafic intrusions depend largely on the proportions of cumulus minerals. The negative correlations between SiO_2 and TiO_2, Fe_2O_3 (Fig. 5a, b) are clearly due to the progressive accumulation of Fe–Ti oxides. The positive

Table 2
Major oxide and trace element concentrations of the Anyi intrusion and country rocks, SW China.

Rock type	Magnetite clinopyroxenite											
Sample	AY-15	AY-18	AY-19	AY-21	AY-22	AY-23	AY-24	AY-25	AY-26	AY-27	AY-28	AY-29
Major oxides (wt.%)												
SiO_2	38.7	36.5	36.7	35.8	37.0	37.1	38.7	38.3	38.8	38.7	38.3	39.7
TiO_2	5.02	5.63	5.98	5.59	5.76	5.96	5.33	5.36	5.3	5.3	5.38	5.1
Al_2O_3	6.4	4.2	5.8	5.3	5.8	6.0	6.3	6.0	5.6	6.0	6.1	6.0
Fe_2O_3T	23.4	26.2	24.4	25.6	25.3	25.9	23.6	24.2	23.6	23.7	24.2	22.7
MnO	0.21	0.23	0.22	0.23	0.22	0.23	0.22	0.22	0.20	0.21	0.21	0.21
MgO	8.96	9.97	8.93	9.34	9.16	8.8	9.09	9.18	9.38	9.24	9.13	9.29
CaO	12.8	14.2	12.2	12.9	12.9	12.2	12.5	12.9	13.1	12.9	12.8	12.9
Na_2O	1.15	0.33	1.08	0.84	0.89	0.97	1.09	1.00	0.95	0.99	0.93	1.18
K_2O	1.11	0.26	0.79	1.39	1.20	1.20	1.39	1.20	1.14	1.24	1.35	1.24
P_2O_5	0.22	0.08	0.16	0.13	0.15	0.17	0.21	0.22	0.15	0.16	0.16	0.17
LOI	2.38	2.93	3.72	3.59	2.36	2.23	2.1	2.09	2.33	2.14	2.15	2.16
Total	99.08	99.34	99.35	99.34	99.19	99.34	99.25	99.20	99.22	99.31	99.32	99.41
Trace elements (ppm)												
Sc	44.7	53.9	44.0	44.8	42.9	39.9	41.9	42.8	44.6	44.3	43.1	44.6
V	724	842	789	870	804	814	670	728	730	744	739	673
Cr	6.7	11.7	5.1	9.2	10.4	19.0	10.6	9.1	12.3	9.3	5.4	20.2
Co	91.7	98.4	99.4	101	104	98.3	82.3	89.2	86.5	102	93.0	89.4
Ni	177	203	48.9	144	131	86.7	160	147	134	151	116	108
Cu	490	563	94.0	484	512	378	541	530	500	472	476	431
Rb	34.3	7.83	28.1	59.0	33.8	34.4	37.5	33.0	32.7	35.9	35.7	36.4
Sr	536	131	313	215	226	404	397	417	240	268	507	225
Y	15.5	11.9	14.8	12.2	13.9	14.8	14.6	15.0	14.0	14.3	13.8	14.3
Zr	178	119	168	139	165	180	178	178	187	175	161	176
Nb	34.7	18.2	29.7	24.8	32.9	32.0	37.6	33.4	32.8	32.2	30.0	33.4
Ba	446	135	301	437	298	364	422	352	320	399	509	354
La	43.6	21.0	35.2	31.8	35.8	39.1	43.0	40.9	37.7	40.9	37.1	40.3
Ce	93.6	49.6	80.1	67.0	76.0	84.1	89.3	87.2	81.3	86.3	79.0	84.6
Pr	11.8	7.0	10.4	8.6	9.8	10.8	11.2	11.4	10.4	10.9	10.1	10.8
Nd	48.5	31.3	43.8	35.9	41.3	44.8	45.5	46.1	42.5	45.0	42.0	44.3
Sm	8.77	6.31	8.17	6.56	7.48	8.00	8.08	8.16	7.68	7.86	7.54	7.83
Eu	2.37	1.72	2.12	1.75	2.02	2.15	2.14	2.14	2.06	2.17	2.13	2.12
Gd	7.10	5.09	6.77	5.45	6.03	6.47	6.51	6.65	6.30	6.49	6.27	6.66
Tb	0.99	0.72	0.95	0.78	0.87	0.92	0.90	0.91	0.86	0.92	0.88	0.90
Dy	3.96	3.12	3.86	3.15	3.48	3.79	3.66	3.81	3.62	3.72	3.52	3.72
Ho	0.74	0.57	0.72	0.57	0.65	0.69	0.67	0.72	0.67	0.68	0.65	0.69
Er	1.93	1.46	1.86	1.51	1.68	1.82	1.81	1.81	1.74	1.85	1.69	1.78
Tm	0.21	0.17	0.20	0.17	0.18	0.21	0.20	0.21	0.20	0.20	0.20	0.19
Yb	1.35	1.03	1.35	1.05	1.13	1.34	1.21	1.33	1.23	1.29	1.23	1.25
Lu	0.18	0.15	0.18	0.15	0.17	0.18	0.17	0.18	0.18	0.18	0.18	0.17
Hf	5.88	4.47	5.75	4.65	5.16	5.92	5.62	5.64	6.26	5.76	5.30	5.45
Ta	2.44	1.46	2.17	1.75	2.29	2.36	2.62	2.42	2.56	2.32	2.18	2.40
Th	4.82	2.14	4.24	4.24	4.43	4.83	5.28	5.03	5.47	5.58	4.47	5.78
U	1.00	0.45	1.05	1.00	0.96	1.00	1.10	1.08	1.03	1.20	0.89	1.26
La/Yb	32.3	20.4	26.1	30.3	31.7	29.2	35.5	30.8	30.7	31.7	30.2	32.2

		Monzogabbro								Monzonite	
AY-30	AY-31	AY-1	AY-2	AY-3	AY-4	AY-5	AY-6	AY-7	AY-8	AY-63	AY-63
Major oxides (wt.%)											Duplicate
38.2	36.5	40.5	40.6	40.8	39.3	39.5	40.4	39.8	39.2	46.4	
5.47	5.85	6.02	5.68	5.86	6.26	6.62	5.95	6.14	6.4	4.01	
6.2	5.9	10.3	11.3	10.8	10.2	8.5	11.6	10.2	10.2	13.5	
23.8	25.8	17.8	17.1	17.7	18.3	19.8	16.5	18.1	18.5	13.3	
0.23	0.25	0.25	0.23	0.24	0.24	0.26	0.23	0.24	0.21	0.21	
8.94	8.42	5.73	5.42	5.54	5.97	6.28	5.33	6.06	6.25	3.74	
13.0	11.7	11.1	11.9	11.0	12.1	11.7	11.8	11.7	11.9	8.56	
1.06	0.84	2.01	2.24	2.00	1.78	1.86	2.07	2.01	1.61	3.00	
1.15	1.23	2.25	1.79	2.41	1.90	1.94	2.13	1.75	1.95	3.96	
0.20	0.23	1.32	1.28	1.26	1.37	1.50	1.47	1.38	1.42	0.90	
2.31	3.78	2.89	2.75	2.7	2.95	2.56	2.84	2.9	2.66	2.79	
99.11	99.32	99.16	99.18	99.20	99.17	99.25	99.12	99.27	99.39	99.39	
Trace elements (ppm)											
41.4	42.9	24.1	22.2	23.2	24.3	27.1	20.6	24.0	24.5	16.7	17.2
723	779	450	413	441	469	544	442	444	464	311	300
11.6	28.4	5.5	3.6	11.2	9.0	3.2	4.0	3.1	5.0	1.2	1.2
97.1	97.9	54.3	54.8	49.8	50.9	50.8	49.1	59.5	54.2	39.1	38.6
103	192	12.2	12.6	15.1	15.6	11.9	11.2	13.2	13.5	8.8	8.9
459	442	74.0	61.8	66.0	65.6	71.9	60.5	129	74.3	47.9	47.4
32.9	78.3	64.5	50.4	69.6	52.9	55.9	55.9	54.1	58.9	93.3	94.2
339	264	1090	1460	1260	1130	594	1320	942	1070	1380	1372
15.3	13.2	28.4	27.5	27.4	29.6	30.2	27.6	28.9	27.5	26.5	25.8

(continued on next page)

Table 2 (*continued*)

		Monzogabbro								Monzonite	
AY-30	AY-31	AY-1	AY-2	AY-3	AY-4	AY-5	AY-6	AY-7	AY-8	AY-63	AY-63
Major oxides (wt.%)											Duplicate
183	169	286	263	286	280	280	277	292	252	345	339
34.6	39.7	69.8	70.1	68.7	75.5	71.1	75.2	49.8	63.7	94.8	94.5
358	526	1960	783	931	661	559	765	660	562	1520	1503
42.4	38.9	102	102	100	106	104	103	101	95.6	117	116
90.2	83.1	208	209	204	220	215	212	210	202	228	225
11.4	10.2	26.2	26.1	25.6	27.9	27.4	26.5	26.9	25.9	26.9	27.0
47.3	42.0	104	104	102	113	111	107	108	106	102	104
8.39	7.18	17.1	16.7	16.7	18.3	18.7	17.7	17.7	17.5	15.8	16.4
2.25	2.06	4.34	4.48	4.25	4.64	4.59	4.45	4.42	4.32	4.47	4.37
6.83	5.88	12.97	13.36	13.09	14.89	14.64	13.53	13.30	13.10	13.11	13.61
0.97	0.85	1.81	1.79	1.81	1.97	2.01	1.86	1.89	1.85	1.75	1.68
3.81	3.24	6.74	6.78	6.63	7.43	7.61	6.97	7.41	7.07	6.27	6.31
0.72	0.60	1.26	1.25	1.23	1.35	1.33	1.26	1.31	1.24	1.19	1.21
1.91	1.61	3.41	3.34	3.35	3.69	3.60	3.37	3.52	3.29	3.33	3.40
0.20	0.18	0.37	0.35	0.34	0.37	0.39	0.36	0.36	0.33	0.35	0.36
1.31	1.17	2.20	2.16	2.14	2.24	2.37	2.23	2.38	2.18	2.28	2.34
0.18	0.16	0.31	0.30	0.31	0.34	0.31	0.31	0.32	0.29	0.31	0.31
5.89	5.18	8.25	7.63	8.30	8.46	8.56	7.97	8.76	7.58	9.09	9.15
2.51	2.89	4.97	5.14	5.00	5.39	5.16	5.55	3.79	4.89	6.26	6.19
5.14	4.81	8.96	8.50	9.70	8.37	8.91	9.74	10.1	7.62	12.4	12.4
1.11	1.05	1.78	1.71	1.94	1.75	1.83	1.96	2.07	1.57	2.51	2.38
32.4	33.2	46.4	47.2	46.7	47.3	43.9	46.2	42.4	43.9	51.3	49.6

Monzonite								Standard			
AY-33	AY-34	AY-32	AY-35	AY-36	AY-61	AY-62	AY-64	AMH-1	GBPG-1	AMH-1	GBPG-1
Major oxides (wt.%)								This study		Recommended	
45.5	46.2	47.3	47.5	49.1	46.0	45.8	44.4				
4.76	4.47	4.05	3.83	3.60	4.39	4.52	4.73				
11.9	13.1	13.4	13.6	14.7	13.3	12.8	12.4				
15.7	14.7	13.4	12.8	11.8	14.2	14.5	15.3				
0.24	0.21	0.20	0.19	0.18	0.21	0.20	0.21				
4.62	4.15	3.85	3.42	3.24	4.07	4.55	4.64				
9.28	9.09	8.68	7.98	7.77	9.62	9.54	10.2				
2.79	3.28	3.32	3.40	3.85	3.06	3.17	3.03				
3.62	3.50	3.90	3.93	4.15	3.42	3.25	2.83				
1.00	0.95	0.87	0.83	0.77	1.03	0.97	1.06				
1.02	1.08	1.06	1.26	1.40	0.85	1.08	1.22				
100.44	100.69	100.00	98.73	100.49	100.14	100.35	49.67				
Trace elements (ppm)											
21.0	20.8	17.4	18.2	15.6	18.5	19.9	18.5	14.7	14.6	13.48	13.93
355	375	318	304	260	343	407	409	118	102	106.4	96.5
5.7	8.1	3.5	2.2	3.0	2.2	3.9	5.7	39.2	176	40.89	181.4
46.2	42.9	38.2	36.0	31.0	42.6	44.0	46.5	19.9	19.7	18.68	19.5
13.3	12.2	9.9	8.6	8.6	10.8	10.8	13.0	38.8	61.3	32.36	59.6
66.6	53.6	46.9	42.5	38.1	55.7	51.6	56.0	28.5	29.1	30.2	30
83.5	90.1	91.1	91.9	96.0	91.4	88.5	76.2	18.6	57.5	18.31	56.2
1070	1290	1300	1390	1500	1500	1090	1200	555	369	545.4	363.5
28.7	28.7	26.8	27.8	26.9	28.9	28.9	28.2	14.4	17.9	16.44	18
307	382	363	383	388	365	389	342	143	255	146	231.8
95.2	102	94.6	100	103	106	101	87.2	8.3	10.1	8.32	9.93
2230	1250	1470	1480	1510	1460	1070	1000	308	904	322.3	908
112	125	120	123	125	125	125	117	15.3	51.3	15.87	52.95
229	245	235	242	240	246	246	232	31.8	98.8	33.03	103.2
28.1	28.5	27.3	27.7	27.4	29.3	28.9	28.0	4.01	11.50	4.21	11.45
111	110	103	105	102	113	111	108	16.3	41.4	17.69	43.3
17.2	16.8	15.4	16.0	15.4	17.2	17.1	16.6	3.56	6.73	3.68	6.79
5.11	4.37	4.33	4.49	4.60	4.50	4.30	4.55	1.12	1.77	1.16	1.79
13.87	14.34	13.21	13.26	12.75	14.50	13.49	13.74	3.11	5.35	3.34	4.74
1.88	1.87	1.68	1.74	1.72	1.88	1.89	1.81	0.52	0.71	0.51	0.6
7.06	6.88	6.46	6.57	6.31	6.87	6.96	6.80	2.58	3.03	2.84	3.26
1.32	1.30	1.20	1.25	1.18	1.27	1.31	1.27	0.55	0.68	0.57	0.69
3.51	3.64	3.36	3.42	3.35	3.64	3.64	3.50	1.50	2.18	1.52	2.01
0.38	0.40	0.37	0.37	0.37	0.39	0.39	0.36	0.20	0.30	0.21	0.3
2.30	2.51	2.25	2.37	2.27	2.44	2.41	2.27	1.28	2.05	1.37	2.03
0.32	0.34	0.32	0.32	0.31	0.33	0.34	0.32	0.19	0.31	0.21	0.31
8.99	9.87	9.40	10.00	9.81	9.66	10.20	9.10	3.52	5.80	3.7	6.07
6.44	6.77	6.44	6.70	6.65	7.05	7.09	6.16	0.60	0.39	0.64	0.4
9.51	14.4	14.8	14.9	15.6	12.7	14.3	13.7	2.34	11.20	2.64	11.23
2.00	3.02	3.03	3.03	3.12	2.69	2.97	2.91	0.81	0.89	0.89	0.9
48.7	49.8	53.3	51.9	55.1	51.2	51.9	51.5				

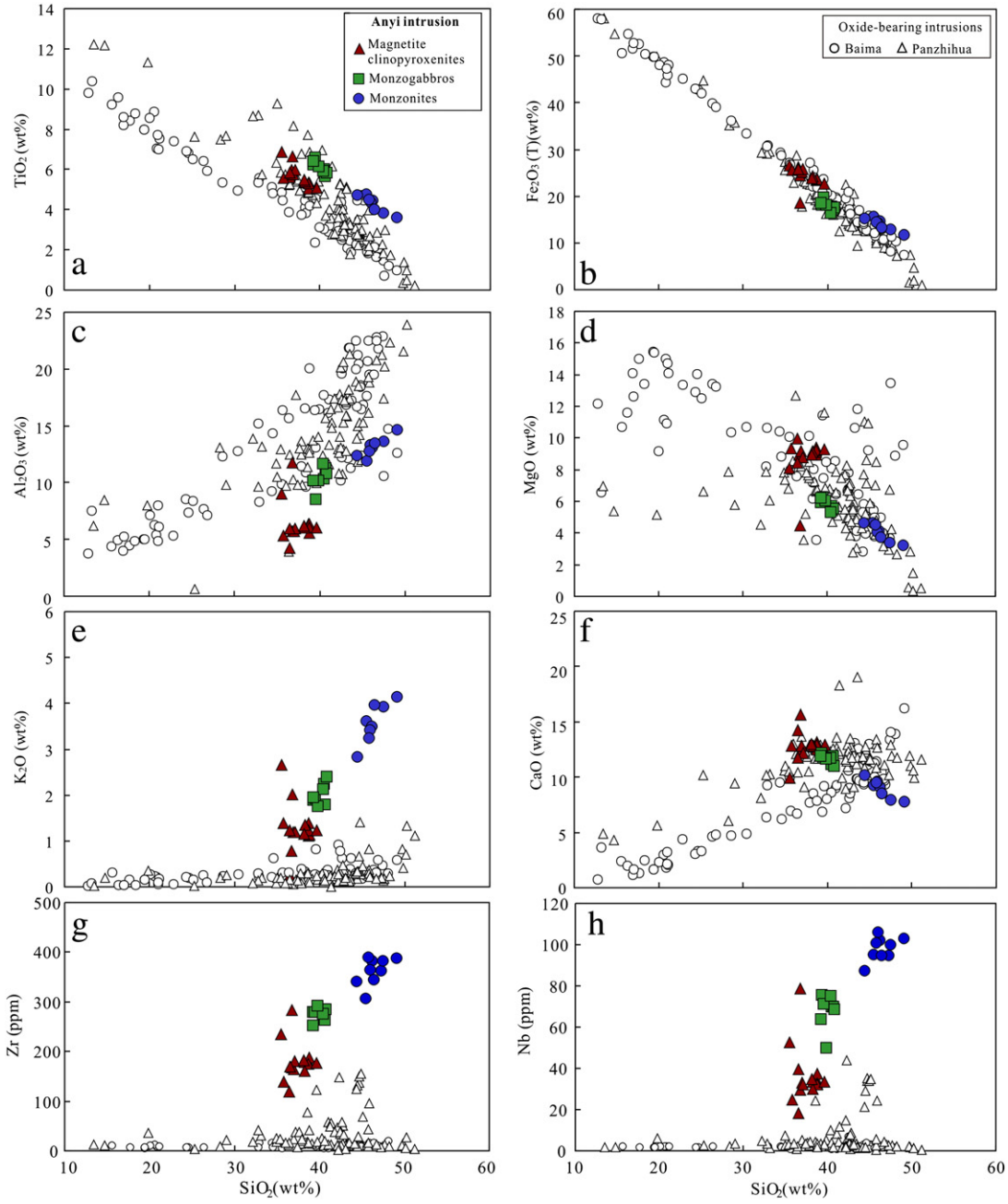

Fig. 5. Harker diagrams showing the variations of major element oxides and trace elements against SiO_2 in rocks of the Anyi intrusion. The Panzhihua and Baima intrusions in the ELIP are from Zhou et al. (2005, 2008), Shellnutt et al. (2009), Zhang et al. (2009).

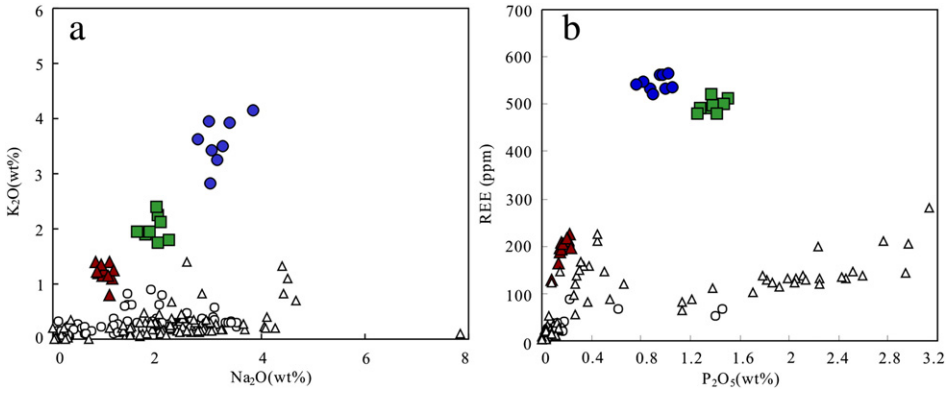

Fig. 6. (a) Plot of Na_2O versus K_2O of rocks from the Anyi intrusion. (b) P_2O_5 contents versus total rare earth element (REE). References are the same as for Fig. 5.

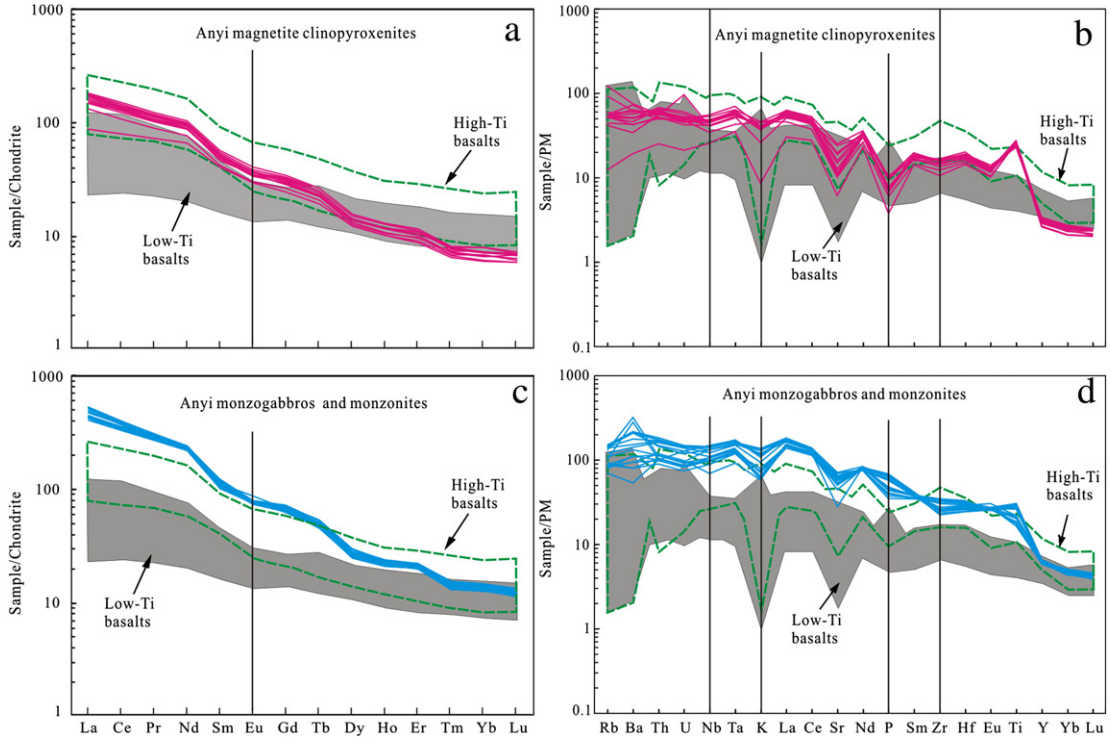

Fig. 7. (a) Chondrite normalized rare earth element patterns of rocks from the Anyi intrusion. (b) Primitive mantle normalized incompatible element patterns of rocks from the Anyi intrusion. Normalization values are from Sun and McDonough (1989). Low-Ti and high-Ti Emeishan basalts are shown for comparison and are from Xu et al. (2001), Xiao et al. (2004) and He et al. (2010).

correlations between SiO_2 and Al_2O_3 can be accounted for by progressive accumulation of feldspars from magnetite clinopyroxenite to monzonite, whereas the relative lower Al_2O_3 contents of the Anyi rocks at comparable SiO_2 compared to those of Panzhihua and Baima intrusions can be explained by less feldspar accumulation in the Anyi intrusion. This is consistent with petrographic observations that there is only ~35–55% of feldspar in the Upper zone monzonites of the Anyi intrusion, in contrast to ~50–70% of feldspar in the Upper zone of the Panzhihua intrusion (Zhou et al., 2005). Besides, accumulation of both orthoclase and plagioclase result in higher K_2O contents of the Anyi intrusion compared to those of Panzhihua and Baima intrusions (Fig. 5e). Considering apatite as the most REE-enriched mineral (Fujimaki, 1986), the late accumulation of apatite results in REE enrichment in monzogabbros and monzonites (Fig. 6b). Additionally, experiments on Fe–Ti oxide/melt partition coefficients have shown that HFSE (Zr, Hf, Nb, Ta) are moderately compatible in the oxides (D = ~1–3), whereas other trace elements (such as REE, Sr, U and Th) are strongly incompatible (of the order of 10^{-5}–10^{-2}, Klemme et al., 2006). It is theoretically possible that accumulation of Fe–Ti oxides could result in elevated ratios of Zr, Nb, Hf, Ta to other trace elements (such as REE Sr, U, Th). Concentrations and ratios of incompatible elements (such as Nb/La, Zr/Sm) of the Panzhihua and Baima intrusions are significantly influenced by the accumulation of Fe–Ti oxides (Fig. 9c–d, Zhang et al., 2009), whereas in the Anyi intrusion, magnetite clinopyroxenites (oxide-rich, ~15–25% Fe–Ti oxides) display similar Zr/Sm ratios with monzonites (oxide-poor, ~5–10% Fe–Ti oxides) (Fig. 9c). Relatively lower Zr/Sm ratios of monzogabbros are inconsistent with oxide accumulation, but may be ascribed to the effect of cumulus apatites (Fig. 9c). Moreover, most of the Anyi rocks display nearly constant Nb/La and only moderate variation of Ti/Sm compared to the Panzhihua

Table 3
Rb–Sr and Sm–Nd isotopic analytical results of the Anyi intrusion.

Sample	Rock type	Rb (ppm)	Sr (ppm)	$^{87}Rb/^{87}Sr$	$(^{87}Sr/^{86}Sr)_0$	$(^{87}Sr/^{86}Sr)_t$	Sm (ppm)	Nd (ppm)	$^{147}Sm/^{144}Nd$	$(^{143}Nd/^{144}Nd)_0$	$(^{143}Nd/^{144}Nd)_t$	εNd (t)
AY-15	Magnetite clinopyroxenite	34.3	536	0.1851	0.708439 ± 7	0.707794	8.77	48.5	0.1093	0.512127 ± 2	0.511952	−7.2
AY-19	Magnetite clinopyroxenite	28.1	313	0.2597	0.70921 ± 7	0.708305	8.17	43.8	0.1127	0.512149 ± 5	0.511968	−6.9
AY-22	Magnetite clinopyroxenite	33.8	226	0.4327	0.70871 ± 6	0.707202	7.48	41.3	0.1094	0.512109 ± 1	0.511934	−7.6
AY-24	Magnetite clinopyroxenite	37.5	397	0.2733	0.709516 ± 7	0.708564	8.08	45.5	0.1073	0.512177 ± 3	0.512005	−6.2
AY-26	Magnetite clinopyroxenite	32.7	240	0.3942	0.709485 ± 7	0.708111	7.68	42.5	0.1092	0.512139 ± 2	0.511964	−7.0
AY-28	Magnetite clinopyroxenite	35.7	507	0.2037	0.709264 ± 5	0.708554	7.54	42				
AY-30	Magnetite clinopyroxenite	32.9	339	0.2808	0.708884 ± 6	0.707905	8.39	47.3				
AY-31	Magnetite clinopyroxenite	78.3	264	0.8582	0.710232 ± 12	0.707241	7.18	42	0.1033	0.512155 ± 3	0.511989	-6.5
AY-2	Monzogabbro	50.4	1460	0.0999	0.70828 ± 7	0.707932	16.7	104	0.0970	0.512116 ± 3	0.511960	−7.1
AY-5	Monzogabbro	55.9	594	0.2723	0.708855 ± 8	0.707906	18.7	111	0.1018	0.51212 ± 2	0.511957	−7.1
AY-8	Monzogabbro	58.9	1070	0.1593	0.708886 ± 4	0.708331	17.5	106	0.0998	0.512109 ± 2	0.511949	−7.3
AY-36	Monzonite	96	1500	0.1852	0.708646 ± 3	0.708001	15.4	102	0.0912	0.51229 ± 2	0.511942	−7.4
AY-62	Monzonite	88.5	1090	0.2349	0.709121 ± 3	0.708302	17.1	111	0.0931	0.512108 ± 2	0.511959	−7.1
AY-64	Monzonite	76.2	1200	0.1837	0.708502 ± 4	0.707862	16.6	108	0.0929	0.51212 ± 1	0.511971	−6.9

Measured isotope ratios (subscript 0) are age-corrected (t) to 247 Ma

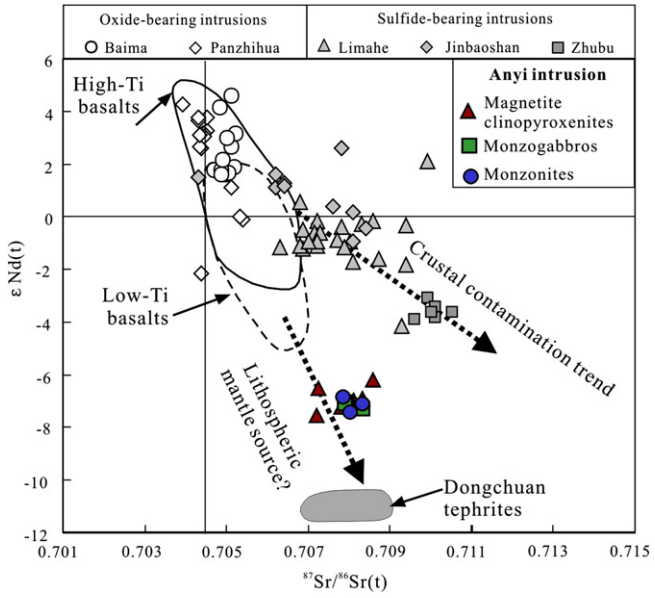

Fig. 8. Plot of εNd values versus initial $^{86}Sr/^{87}Sr$ ratios of rocks from the Anyi intrusion (T = 247 Ma). Other oxide-bearing and sulfide-bearing intrusions in ELIP refer to Zhou et al. (2005, 2008), Shellnutt et al. (2009), Tao et al. (2007, 2008), Zhang et al. (2009). The compositional range of low-Ti and high-Ti basalts in the ELIP is from Xu et al. (2001), Xiao et al. (2004), He et al. (2010). The Dongchuan tephrites are from Song et al. (2008).

and Baima intrusions, which suggests that the effect of cumulus Fe–Ti oxides is not significant for most of HFSE of the Anyi intrusion (Fig. 9d). The relatively good positive correlations between SiO_2 and Zr, Nb (Fig. 5) are also consistent with only weak effect of cumulus Fe–Ti oxides. Thus, ratios between HFSE and other incompatible elements can be used as tracers of crustal contamination or source of magma.

Variable degrees of crustal assimilation are commonly expected for mantle-derived magmas migrating through continental crust to the surface (Carlson, 1991; Hawkesworth et al., 1984; Hergt et al., 1991; Mahoney, 1988). Nd and Sr isotope compositions and ratios between HFSE in mafic rocks may be indicative of crustal contamination in an open magma system. The negative εNd (247 Ma) values of the Anyi rocks ranging from −6.2 to −7.6 and their moderately high $^{86}Sr/^{87}Sr$(247 Ma) ratios varying from 0.7072 to 0.7086 (Table 3) might reflect significant crustal contamination. However, it is evident that trace element concentrations and ratios are controlled primarily by their mantle source, rather than by crustal contamination. For example, the significantly low Th/Nb and Zr/Nb ratios (0.1–0.2 and 3.2–6.5, respectively) of the Anyi rocks compared to crustal rocks (0.08–0.42 and 9.4–40, respectively, Rudnick and Fountain, 1995) are not compatible with extensive crustal contamination. Instead, the Th/Nb and Zr/Nb ratios of the Anyi rocks are similar to those of OIB (0.06 and 4.2, respectively) (Sun and Mcdonough, 1989) (Fig. 10a). The relatively high and homogenous Nb/La ratios (0.49–1.02) of the Anyi rocks also indicate only weak crustal contamination. In addition, if the negative εNd (247 Ma) values of the Anyi rocks (as much as −6.2 to −7.6) resulted from extensive crustal contamination, these rocks should display strong negative Nb anomalies in the primitive normalized trace element patterns. However, most of the Anyi samples display no or only weak negative Nb anomalies relative to Th and La as shown in Fig. 7. Moreover, large variations of 1/Sr, La/Yb and Th/Yb and small variations of εNd(t) and $^{86}Sr/^{87}Sr$(t) are also inconsistent with extensive crustal assimilation (Fig. 10b–d). Finally, both Nb/La and Th/Nb ratios of the Anyi

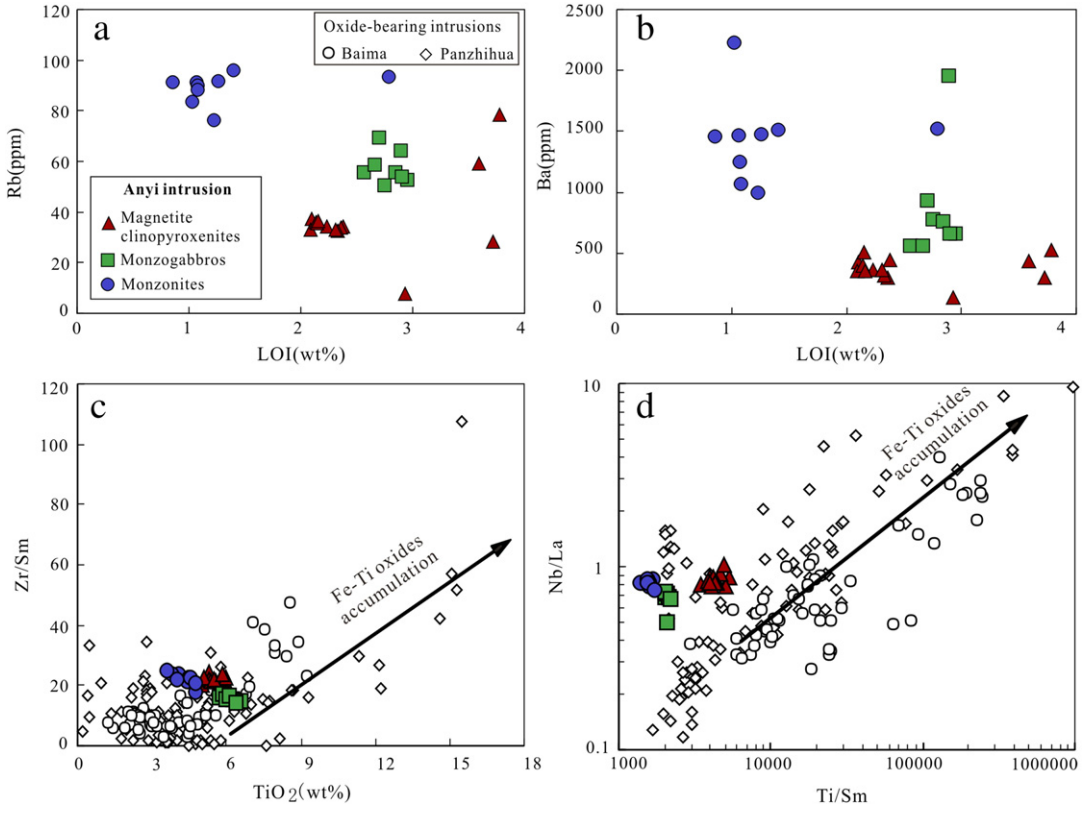

Fig. 9. (a–b) Plots of LOI (loss on ignition) versus Rb and Ba of rocks from the Anyi intrusion. (c) Plot of TiO_2 versus Zr/Sm. It is worth noting that the Anyi rocks do not follow the Fe–Ti oxide accumulation trend defined by the Panzhihua and Baima intrusion. (d) Plot of Ti/Sm versus Nb/La. The Anyi rocks also do not follow the Fe–Ti oxide accumulation trend. References are the same as for Fig. 5.

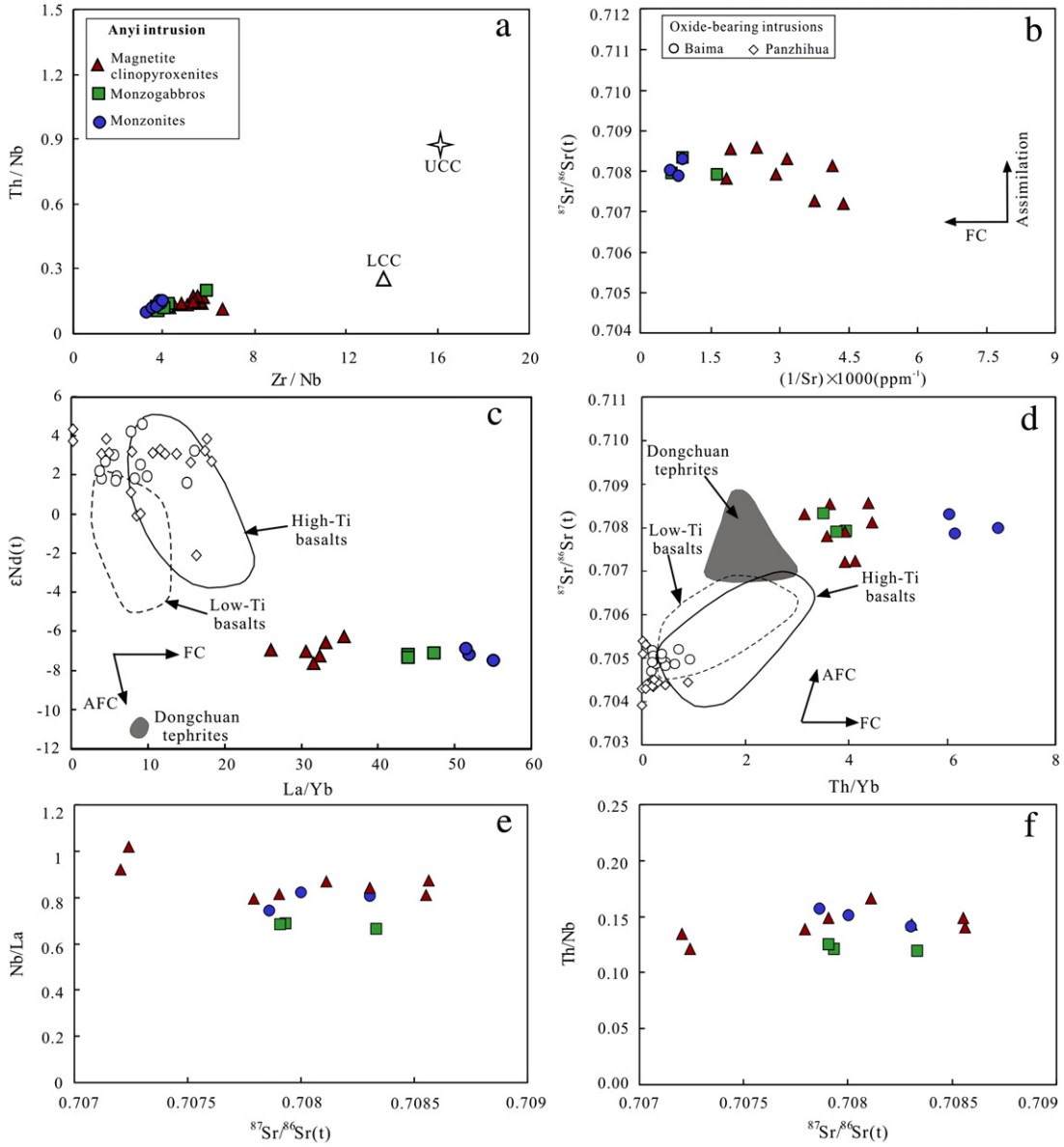

Fig. 10. (a) Plot of Zr/Nb versus Th/Nb of the Anyi intrusion, Upper continental crust (UCC) and lower continental crust (LCC) are from Rudnick and Fountain (1995). (b) 1/Sr versus $^{86}Sr/^{87}Sr$. (c) Plot of εNd values versus La/Yb ratios of rocks from the Anyi intrusion. (d) $^{86}Sr/^{87}Sr$ versus Th/Yb ratios of rocks from the Anyi intrusion. (e) Plot of $^{86}Sr/^{87}Sr$ versus Nb/La. (f) Plot of $^{86}Sr/^{87}Sr$ versus Th/Nb. Compositional range of the low-Ti and high-Ti basalts in the ELIP is from Xu et al. (2001), Xiao et al. (2004), He et al. (2010). The Dongchuan tephrites are from Song et al. (2008). The Panzhihua and Baima intrusions in the ELIP are also shown for comparison and are from Zhou et al. (2005, 2008), Shellnutt et al. (2009), Zhang et al. (2009).

rocks keep nearly constant with variation of $^{86}Sr/^{87}Sr$ (t) ratios (Fig. 10e, f). Therefore, we conclude that, although minor crustal contamination may occur, it was not an important factor controlling the trace element ratios and Sr–Nd isotope compositions of the Anyi intrusion. Instead, the trace element ratios and Sr–Nd isotope values of the Anyi rocks mainly reflect the characteristics of their mantle source.

6.3. Nature of mantle source

Recent geochemical studies of the Emeishan flood basalts argued that the high-Ti basalts are products of deep melting of the plume head, whereas the low-Ti basalts were generated from shallow melting of the plume head with significant lithospheric overprint (Chung and Jahn, 1995; He et al., 2010; Song et al., 2001; Xiao et al., 2004; Xu et al., 2001). Besides, the contemporaneous Fe–Ti oxide-bearing intrusions (such as Panzhihua, Baima) are genetically related to the high-Ti basalts, and the Ni–Cu sulfide-bearing intrusions (such as Jinaoshan, Limahe and Zhubu) likely share a common mantle source with the low-Ti basalts in the ELIP (Zhou et al., 2008). Compared with these flood basalts and intrusions, the Anyi intrusion is characterized by high concentrations of incompatible elements, high LREE/HREE ratios (La/Yb = 20.4–55.1, Table 2), and very low εNd (−6.2 to −7.6) (Fig. 8). These characteristics suggest that the Anyi intrusion was derived from an extremely enriched mantle source, rather than the mantle plume or asthenosphere. Possible enriched mantle sources include (a) ancient metasomatized lithospheric mantle with hydrous minerals (Boyd and Mertzman, 1987; Boyd and Nixon, 1975; Maury et al., 1992; O'Reilly and Griffin, 1988; Waters and Erlank, 1988), or (b) a mantle source mixed between garnet pyroxenite and spinel peridotite (Hirschmann and Stolper, 1996). An evaluation of these two alternatives will be given below.

The metasomatism model involves infiltration of the depleted upper mantle by small-degree metasomatic melts leading to enrichment of incompatible elements (Pilet et al., 2005, 2008). Metasomatism processes would generate enriched peridotite sources with hydrous minerals

(such as amphibole and phlogopite), which can develop low εNd and high $(^{87}Sr/^{86}Sr)_i$ comparable to those of the Anyi intrusion, provided that there is enough time for the evolution of isotopic signatures after the metasomatic event. However, this metasomatized model encountered the following problems when applied to the Anyi intrusion. (1) Experiments on phlogopite/melt partition coefficients have shown that Rb, Ba and K are moderately compatible for phlogopite (D = ~2–4), whereas other trace elements (such as Th, U and REE) are strongly incompatible (of the order of 10^{-2}, LaTourrette et al., 1995). In addition, most trace elements are moderately incompatible for amphibole. Therefore, concentrations of trace elements in amphibole are generally higher than those in anhydrous minerals, such as olivine and pyroxene, in the metasomatized mantle. If the ancient metasomatized lithospheric mantle with hydrous minerals is the direct source of the Anyi intrusion, residues of amphibole and phlogopite after a small degree of partial melting may account for the negative K anomalies of the Anyi intrusion on multi-element spider diagrams (Fig. 7b, d, Class and Goldstein, 1997; Ionov et al., 1997). However, amphibole and phlogopite residues in magma source can equally generate depletion of Rb and Ba in the melts because of the high partition coefficients of Rb and Ba in phlogopite (D = ~2–4, LaTourrette et al., 1995), a feature not observed in the Anyi intrusion. (2) The Anyi intrusion was formed after the peak of tholeiitic volcanism in the ELIP (~260 Ma) and displays depletion of heavy REE (Sm/Yb = 6.0–8.2), suggesting a garnet-bearing mantle source. If a garnet-bearing metasomatized lithospheric mantle is the source of the Anyi intrusion, it is difficult to explain how this metasomatized lithospheric mantle could have survived from the large scale plume-related magma activity (~260 Ma), because most of the fusible constituents in the lower part of sub-continental lithospheric mantle (SCLM) would be melted and extracted due to underplating (or ascending) of mantle plume.

Another possible resolution of this conflict is that the Anyi intrusion may be associated with the melting of a mantle source mixed between garnet pyroxenite and spinel peridotite. Partial melting of garnet pyroxenite blocks or veins also resulted in melting of ambient spinel peridotite inevitably. However, the "garnet signature" in the Anyi intrusion shows more significant melting of the garnet pyroxenites. Garnet is a solidus phase to substantially lower pressure (~1.5 GPa) in the pyroxenite, which may occur as blocks or veins in the spinel peridotite subcontinental lithospheric mantle at shallow depth (Hirschmann and Stolper, 1996). The garnet pyroxenite blocks or veins in the shallow lithospheric mantle may be produced by the reaction of subduction-related melts with lithospheric peridotites (Herzberg, 2006; Sobolev et al., 2005; Yaxley and Green, 1998). Partial melting of subducted oceanic slab in the Neoproterozoic resulted in adakitic plutons, such as the Datian and Dajianshan plutons, along the west margin of the Yangtze Block subduction, and left garnet as a residue in the source (Zhao et al., 2008; Zhou et al., 2002b). Such ascending adakitic melts would react with olivine and produce garnet pyroxenites within the lithospheric mantle (Herzberg, 2006; Rapp et al., 1999; Sobolev et al., 2005; Yaxley and Green, 1998). This kind of garnet pyroxenite is predicted to be enriched in most incompatible trace elements (e.g., Rb, K, Na, and LREE) and can develop enriched Sr, Nd isotopic compositions after long-term radiogenic decay. Melting of such ancient garnet pyroxenite blocks or veins in the lithospheric mantle would produce Fe-rich melts with enriched incompatible trace elements and Sr–Nd isotopic compositions (Yaxley and Green, 1998). We speculate that the Anyi intrusion is associated with partial melting of a mantle source mixed between garnet pyroxenite and spinel peridotite in the lithospheric mantle beneath the Yangtze Block. This hypothesis is supported by highly enriched incompatible trace elements and Sr–Nd isotope compositions and Fe–Ti enriched parental magma of the Anyi intrusion. This hypothesis is also consistent with the low $^3He/^4He$ and $^{40}Ar/^{36}Ar$ ratios of Fe–Ti oxide-bearing layered intrusions in the central ELIP, which are also considered to be related to the infiltration of subduction-related melts and fluids into lithospheric peridotites during the Neoproterozoic (Hou et al., 2011).

However, it is still an open question how these Neoproterozoic garnet pyroxenites survived from the main pulse of tholeiitic volcanism of the ELIP that occurred at ~260 Ma. Xiao et al. (2004) proposed that SCLM melting was terminated after the peak tholeiitic magmatism at ~260 Ma, because SCLM would become depleted and refractory after extraction of the low-Ti basalts. However, it is difficult that the fusible constituents within the SCLM were extracted completely during such a short time (~1 Ma), because SCLM is commonly very thick (>100 km).

6.4. Origin of the delayed mafic magmatism and its significance

Comparative studies have indicated that the large igneous provinces genetically associated with mantle plumes commonly have three eruptive phases: (1) an initial eruptions of relatively small volume transitional-alkaline basalts, (2) the main phase of rapid eruptions of large volume tholeiitic basalt magma and in some cases, silicic magma, and (3) a waning and protracted activity of mafic magmas, in many cases, with increasing silicic components (Bryan and Ernst, 2008; Bryan et al., 2002; Jerram and Widdowson, 2005; White and McKenzie, 1995).

It has been demonstrated that the main pulse of tholeiitic volcanism of the ELIP occurred at ~260 Ma within no more than one million years (Ali et al., 2002; He et al., 2007). Several spatially associated mafic–ultramafic intrusions (such as Panzhihua, Baima, Hongge, Xinjie, Limahe, Jinbaoshan, Baimazhai, Zhubu) contemporaneous with the Emeishan basalts (~260 Ma) were regarded as the results of the same igneous event (Fig. 1) (Wang and Zhou, 2006; Zhong and Zhu, 2006; Zhou et al., 2002c, 2005, 2008). The tephrites at the base of the Dongchuan Emeishan basalt sequence represent the earliest eruption resulting from the melting of the metasomatized base of the Yangtze continental lithospheric mantle during plume–lithosphere interaction (Song et al., 2008a). A-type granites and syenites with ages of ~260 Ma are contemporaneous with the mafic–ultramafic layered intrusions, and are attributed to thorough differentiation of underplated basaltic magmas (Xu et al., 2010; Zhong et al., 2007, 2009), By contrast, ~238 Ma rhyolitic tuff at the top of the Emeishan flood basalt sequence (Binchuan) and ~251 Ma Ailanghe I-type granites occurring in the central ELIP were considered to have been formed by the melting of the lower crust of the Yangtze Block (Xu et al., 2008; Zhong et al., 2007). Obviously, such delayed felsic magmatism needs episodic basaltic magma underplating to provide enough heat for crustal melting. The Anyi (~247 Ma) and Cida mafic–ultramafic intrusion (~243 Ma) and Baima mafic dykes (~242 Ma) clearly demonstrate that a weak mantle-derived magmatism indeed occurred in the central ELIP after the peak magmatism of the Emeishan mantle plume (Fig. 1) (Luo et al., 2013; Shellnutt et al., 2008). The postdated mafic magma associated with the Anyi and Cida intrusions likely played an important role in supplying heat for crustal melting and generation of the delayed I-type magmas. However, how the postdated mafic magmas were generated is still not well understood.

The OIB-like trace element patterns, coupled with near primitive εNd (0.32–2.7) and $(^{87}Sr/^{86}Sr)_i$ (0.70485–0.7064) of Baima mafic and Cida mafic–ultramafic rocks suggest a plume head origin (Luo et al., 2013; Shellnutt et al., 2008). It implies that the Emeishan plume persisted for ~20 Myrs beneath the western Yangtze Block. Similarly, we speculate that the mantle plume is the potential heat source that produced the magma associated with the Anyi intrusion by partial melting of the mantle source mixed between garnet pyroxenite and spinel peridotite in the shallow lithospheric mantle beneath the Yangtze Block. The possible mechanisms to cause shallow melting of the lithosphere include (a) simple conductive heating from the deep-seated plume to the shallow lithosphere, and (b) conductive heating combined with lithosphere thinning due to upwelling of the Emeishan mantle plume. According to the conductive heating modeling performed by Gibson et al. (2006), conductive heating is a relatively slow process, and only the base of the lithosphere (>100 km) can be heated on

timescales of 20 Myrs if the initial lithosphere thicknesses were 130 and 165 km, respectively. A similar conclusion reached by Xu et al (2008) shows that conductive heating at the base of 150 km thick lithosphere raises the temperature of lithosphere over a depth of only ~40 km in a 20 Myr time interval. Therefore, we propose that simple conductive heating from the deep seated mantle plume to the lithosphere is not enough to induce melting of the shallow lithosphere.

Davies (1994) conducted a simplified semianalytic theory which describes the process of lithosphere thinning through thermomechanical erosion by a hot mantle upwelling or plume. His results demonstrated that if the upwelling persists for 10–20 Myrs under 120 km thick continental lithosphere, a substantial thinning by thermal erosion can occur. This mechanism may indeed have operated in the Emeishan LIP. It has been postulated that a lens-shaped seismically anomalous body at the depth of 80–120 km may represent the head of the fossil mantle plume (Xu and He, 2007; Xu et al., 2004). If this is true, the plume head must have risen to a depth of ~80 km. This implies that the mantle lithosphere beneath the west Yangtze Block is significantly thinned since the initial lithosphere thickness was likely greater than 100 km. The relatively "thin" lithosphere (<100 km) is more effectively warmed up in 20 Myrs by conductive heating (Xu et al., 2008). Therefore, we prefer the model of conductive heating combined with lithosphere thinning to explain the delayed mafic magmatism of the Anyi intrusion. In this model, the plume–lithosphere interaction process may persist for more than 10 Myrs. The removal of the lower part of lithospheric materials through thermomechanical erosion enhanced the conduction of heat from the plume into the overlying shallow lithosphere. The shallow lithosphere is warmed up after a short time lag (13 Ma) relative to the plume impact (~260 Ma) during plume–lithosphere interaction. Melting of the mixed garnet pyroxenite/spinel peridotite source would result in the generation of Fe-rich melts and formation of the Anyi intrusion and its Fe–Ti oxide ore. On the other hand, the delayed melting of the plume-head resulted in the formation of the Baima mafic dykes (~242 Ma) and Cida mafic–ultramafic rocks (~243 Ma) in the central ELIP (Luo et al., 2013; Shellnutt et al., 2008).

7. Conclusions

The Anyi intrusion display relatively younger emplacement age (247 ± 3 Ma) and may represent the postdated mafic magmatism after the main pulse of tholeiitic volcanism of the ELIP (~260 Ma). The high LREE/HREE ratios (La/Yb = 20.4–55.1) and extremely low εNd values (-6.2 to -7.6) of the Anyi intrusion can be explained by the partial melting of the mantle source mixed between garnet pyroxenite and spinel peridotite in the shallow lithosphere caused by conductive heating combined with lithosphere thinning during plume–lithosphere interaction. The delayed mafic magma associated with the formation of the Anyi intrusion may play an important role in supplying heat for crustal melting and the generation of the delayed I-type magma in the ELIP.

Acknowledgments

The authors acknowledge the constructive reviews by Kwan-Nang Pang and an anonymous referee and the editorial handling by Zhao-Chong Zhang. We also would like to thank Hu Jing, Xiao Fang and Xie Wei for their efforts in trace element, Sr–Nd isotope analysis and Zircon U–Pb dating works. This study was funded by the National Basic Research Program of China (2012CB416804) and research grants from the State Key Laboratory of Ore Deposit Geochemistry (SKLODG-ZY125-06) and NSFC (40730420 and 41373042) to Xie-Yan Song and Song-Yue Yu.

References

Ali, J.R., Thompson, G.M., Song, X.-Y., 2002. Emeishan basalts (SW China) and the 'end-Guadalupian' crisis: magnetobiostratigraphic constraints. J. Geol. Soc. 159, 21–29.

Bai, Z.-J., Zhong, H., Naldrett, A.J., Zhu, W.-G., Xu, G.-W., 2012. Whole-rock and mineral composition constraints on the genesis of the giant Hongge Fe–Ti–V oxide deposit in the Emeishan Large Igneous Province, Southwest China. Econ. Geol. 107, 507–524.

Black, L.P., Kamo, S.L., Allen, C.M., Aleinikoff, J.N., Davis, D.W., Korsch, R.J., Foudoulis, C., 2003. TEMORA 1: a new zircon standard for Phanerozoic U–Pb geochronology. Chem. Geol. 200, 155–170.

Boyd, F.R., Mertzman, S.A., 1987. Composition and structure of the Kaapvaal lithosphere, southern Africa. In: Mysen, B.O. (Ed.), Magmatic Processes: Physicochemical Principles. Geochemical Society Special Publication, 1, pp. 13–24.

Boyd, F.R., Nixon, P.H., 1975. Origins of the ultramafic nodules from some kimberlites of northern Lesotho and the Monastery Mine, South Africa. Phys. Chem. Earth. 9, 431–454.

Bryan, S.E., Ernst, R.E., 2008. Revised definition of Large Igneous Provinces (LIPs). Earth Sci. Rev. 86, 175–202.

Bryan, S.E., Riley, T.R., Jerram, D.A., Leat, P.T., Stephens, C.J., 2002. Silicic volcanism: an under-valued component of large igneous provinces and volcanic rifted margins. In: Menzies, M.A., Klemperer, S.L., Ebinger, C.J., Baker, J. (Eds.), Magmatic Rifted Margins. Geological Society of America Special Paper, 362, pp. 99–118.

Carlson, R.W., 1991. Physical and chemical evidence on the cause and source characteristics of flood basalt volcanism. Aust. J. Earth Sci. 38, 525–544.

Chung, S.-L., Jahn, B.-M., 1995. Plume–lithosphere interaction in generation of the Emeishan flood basalts at the Permian–Triassic boundary. Geology 23, 889–892.

Class, C., Goldstein, S.L., 1997. Plume–lithosphere interactions in the ocean basins: constraints from the source mineralogy. Earth Planet. Sci. Lett. 150, 245–260.

Compston, W., Williams, I.S., Kirschvink, J.L., Zhang, Z., Ma, G., 1992. Zircon U–Pb ages for the Early Cambrian time-scale. J. Geol. Soc. 149, 171–184.

Courtillot, V.E., Renne, P.R., 2003. On the ages of flood basalt events. C.R. Geosci. 335, 113–140.

Davies, G.F., 1994. Thermomechanical erosion of the lithosphere by mantle plumes. J. Geophys. Res. 99, 15709–15722.

Fujimaki, H., 1986. Partition coefficients of Hf, Zr, and REE between zircon, apatite, and liquid. Contrib. Mineral. Petrol. 94, 42–45.

Geological Unit, Panxi, 1984. Mineralization and exploration forecasting of V–Ti magnetite deposits in the Panzhihua–Xichang Region (in Chinese).

Gibson, S.A., Thompson, R.N., Day, J.A., 2006. Timescales and mechanisms of plume–lithosphere interactions: 40Ar/39Ar geochronology and geochemistry of alkaline igneous rocks from the Paraná–Etendeka large igneous province. Earth Planet. Sci. Lett. 251, 1–17.

Hawkesworth, C.J., Rogers, N.W., Vancalsteren, P.W.C., 1984. Mantle enrichment processes. Nature 311, 331–335.

He, B., Xu, Y.-G., Huang, X.-L., Luo, Z.-Y., Shi, Y.-R., Yang, Q.-J., Yu, S.-Y., 2007. Age and duration of the Emeishan flood volcanism, SW China: geochemistry and SHRIMP zircon U–Pb dating of silicic ignimbrites, post-volcanic Xuanwei Formation and clay tuff at the Chaotian section. Earth Planet. Sci. Lett. 255, 306–323.

He, Q., Xiao, L., Balta, B., Gao, R., Chen, J., 2010. Variety and complexity of the Late-Permian Emeishan basalts: reappraisal of plume–lithosphere interaction processes. Lithos 119, 91–107.

Hergt, J.M., Peate, D.W., Hawkesworth, C.J., 1991. The petrogenesis of Mesozoic Gondwana low-Ti flood basalts. Earth Planet. Sci. Lett. 105, 134–148.

Herzberg, C., 2006. Petrology and thermal structure of the Hawaiian plume from Mauna Kea volcano. Nature 444, 605–609.

Hirschmann, M.M., Stolper, E.M., 1996. A possible role for garnet pyroxenite in the origin of the "garnet signature" in MORB. Contrib. Mineral. Petrol. 124, 185–208.

Hooper, P.R., 1997. The Columbia River flood basalt province: current status. In: Mahoney, J.J., Coffin, M.F. (Eds.), Large Igneous Provinces: Continental, Oceanic, and Planetary Flood Volcanism. American Geophysical Union Monograph, 100, pp. 1–27 (Washington, DC).

Hou, T., Zhang, Z., Ye, X., Encarnacion, J., Reichow, M.K., 2011. Noble gas isotopic systematics of Fe–Ti oxide ore-related mafic–ultramafic layered intrusions in the Panxi area, China: the role of recycled oceanic crust in their petrogenesis. Geochim. Cosmochim. Acta 75, 6727–6741.

Ionov, D.A., Griffin, W.L., O'Reilly, S.Y., 1997. Volatile-bearing minerals and lithophile trace elements in the upper mantle. Chem. Geol. 141, 153–184.

Jerram, D.A., Widdowson, M., 2005. The anatomy of Continental Flood Basalt Provinces: geological constraints on the processes and products of flood volcanism. Lithos 79, 385–405.

Karlstrom, L., Richards, M., 2011. On the evolution of large ultramafic magma chambers and timescales for flood basalt eruptions. J. Geophys. Res. 116, 1–13.

Klemme, S., Günther, D., Hametner, K., Prowatke, S., Zack, T., 2006. The partitioning of trace elements between ilmenite, ulvospinel, armalcolite and silicate melts with implications for the early differentiation of the moon. Chem. Geol. 234, 251–263.

LaTourrette, T., Hervig, R.L., Holloway, J.R., 1995. Trace element partitioning between amphibole, phlogopite, and basanite melt. Earth Planet. Sci. Lett. 135, 13–30.

Ludwig, K.R., 2001. User's manual for Isoplot/Ex (rev. 2.49): a geochronological toolkit for Microsoft Excel. Berkeley Geochronology Center, Special Publication, 1a 55.

Luo, W.-J., Zhang, Z.-C., Hou, T., Wang, M., 2013. Geochronology–geochemistry of the Cida bimodal intrusive complex, central Emeishan large igneous province, southwest China: petrogenesis and plume–lithosphere interaction. Int. Geol. Rev. 55, 88–114.

Mahoney, J.J., 1988. Deccan Traps. In: MacDougall, J.D. (Ed.), Continental Flood Basalts. Kluwer Academic, Dordrecht, pp. 151–194.

Maury, R.C., Defant, M.J., Joron, J.-L., 1992. Metasomatism of the sub-arc mantle inferred from trace elements in Philippine xenoliths. Nature 360, 661–663.

O'Reilly, S.Y., Griffin, W.L., 1988. Mantle metasomatism beneath western Victoria, Australia: I. Metasomatic processes in Cr–diopside lherzolites. Geochim. Cosmochim. Acta 52, 433–447.

Pilet, S., Hernandez, J., Sylvester, P., Poujol, M., 2005. The metasomatic alternative for ocean island basalt chemical heterogeneity. Earth Planet. Sci. Lett. 236, 148–166.
Pilet, S., Baker, M.B., Stolper, E.M., 2008. Metasomatized lithosphere and the origin of alkaline lavas. Science 320, 916–919.
Qi, L., Hu, J., Gregoire, D.C., 2000. Determination of trace elements in granites by inductively coupled plasma mass spectrometry. Talanta 51, 507–513.
Rapp, R.P., Shimizu, N., Norman, M.D., Applegate, G.S., 1999. Reaction between slab-derived melts and peridotite in the mantle wedge: experimental constraints at 3.8 GPa. Chem. Geol. 160, 335–356.
Richards, M.A., Duncan, R.A., Courtillot, V.E., 1989. Flood basalts and hot-spot tracks: plume heads and tails. Science 246, 103–107.
Rudnick, R., Fountain, D.M., 1995. Nature and composition of the continental crust: a lower crustal perspective. Rev. Geophys. 33, 267–309.
Saunders, A.D., Fitton, J.G., Kerr, A.C., Norry, M.J., Kent, R.W., 1997. The North Atlantic Igneous Province. In: Mahoney, J.J., Coffin, M.F. (Eds.), Large Igneous Provinces: Continental, Oceanic, and Planetary Flood Volcanism. American Geophysical Union Monograph, 100, pp. 45–93 (Washington, DC).
Shellnutt, J.G., Zhou, M.-F., Yan, D.-P., Wang, Y., 2008. Longevity of the Permian Emeishan mantle plume (SW China): 1 Ma, 8 Ma or 18 Ma? Geol. Mag. 145, 373–388.
Shellnutt, J.G., Zhou, M.-F., Zellmer, G.F., 2009. The role of Fe–Ti oxide crystallization in the formation of A-type granitoids with implications for the Daly gap: an example from the Permian Baima igneous complex, SW China. Chem. Geol. 259, 204–217.
Sichuan, 1991. Regional geology of Sichuan province. Geological Memoirs, Series, 23. Geologic Press, Beijing (in Chinese).
Sobolev, A.V., Hofmann, A.W., Sobolev, S.V., Nikogosian, I.K., 2005. An olivine-free mantle source of Hawaiian shield basalts. Nature 434, 590–597.
Song, X.-Y., Zhou, M.-F., Hou, Z.-Q., Cao, Z.-M., Wang, Y.-L., Li, Y., 2001. Geochemical constraints on the mantle source of the Upper Permian Emeishan Continental Flood Basalts, Southwestern China. Int. Geol. Rev. 43, 213–225.
Song, X.-Y., Zhou, M.-F., Cao, Z.-M., Sun, M., Wang, Y.-L., 2003. Ni–Cu–(PGE) magmatic sulfide deposits in the Yangliuping area, Permian Emeishan igneous province, SW China. Miner. Depos. 38, 831–843.
Song, X.-Y., Zhong, H., Zhou, M.-F., Tao, Y., 2005. Magmatic sulfide deposits in the Permian Emeishan Large Igneous Province, SW China. In: Mao, J.W., Bierlein, F.P. (Eds.), Mineral Deposit Research: Meeting the Global Challenge. Springer, Berlin.
Song, X.-Y., Qi, H.-W., Robinson, P.T., Zhou, M.-F., Cao, Z.-M., Chen, L.-M., 2008a. Melting of the subcontinental lithospheric mantle by the Emeishan mantle plume: evidence from the basal alkaline basalts in Dongchuan, Yunnan, Southwestern China. Lithos 100, 93–111.
Song, X.-Y., Zhou, M.-F., Tao, Y., Xiao, J.-F., 2008b. Controls on the metal compositions of magmatic sulfide deposits in the Emeishan large igneous province, SW China. Chem. Geol. 253, 38–49.
Song, X.-Y., Keays, R.R., Xiao, L., Qi, H.-W., Ihlenfeld, C., 2009. Platinum-group element geochemistry of the continental flood basalts in the central Emeisihan Large Igneous Province, SW China. Chem. Geol. 262, 246–261.
Song, X.-Y., Qi, H.-W., Hu, R.-Z., Chen, L.-M., Yu, S.-Y., Zhang, J.-F., 2013. Formation of thick stratiform Fe–Ti oxide layers in layered intrusion and frequent replenishment of fractionated mafic magma: evidence from the Panzhihua intrusion, SW China. Geochem. Geophys. Geosyst. 14, 712–732.
Sun, S.S., McDonough, W.F., 1989. Chemical and isotopic systematics of oceanic basalts: implications for mantle composition and processes. In: Saunders, A.D., Norry, M.J. (Eds.), Magmatism in the Ocean Basins. Geological Society Special Publication, 42, pp. 313–345.
Tao, Y., Li, C., Hu, R., Ripley, E.M., Du, A., Zhong, H., 2007. Petrogenesis of the Pt–Pd mineralized Jinbaoshan ultramafic intrusion in the Permian Emeishan Large Igneous Province, SW China. Contrib. Mineral. Petrol. 153, 321–337.
Tao, Y., Li, C., Song, X.-Y., Ripley, E.M., 2008. Mineralogical, petrological, and geochemical studies of the Limahe mafic–ultramatic intrusion and associated Ni–Cu sulfide ores, SW China. Miner. Depos. 43, 849–872.
Wang, C., Zhou, M.-F., 2006. Genesis of the Permian Baimazhai magmatic Ni–Cu–(PGE) sulfide deposit, Yunnan, SW China. Miner. Depos. 41, 771–783.
Waters, F.G., Erlank, A.J., 1988. Assessment of the vertical extent and distribution of mantle metasomatism below Kimberley South Africa. J. Petrol. 185–204 (Special Volume).
White, R.S., McKenzie, D., 1995. Mantle plumes and flood basalts. J. Geophys. Res. 100, 17543–17585.
Williams, I.S., 1998. U–Th–Pb geochronology by ion microprobe. In: McKibben, M.A., Shanks III, W.C., Ridley, W.I. (Eds.), Applications of Microanalytical Techniques to Understanding Mineralizing Processes. Reviews in Economic Geology, 7, pp. 1–35.
Xiao, L., Xu, Y.G., Chung, S.L., He, B., Mei, H.J., 2003. Chemostratigraphic correlation of Upper Permian lavas from Yunnan province, China: extent of the Emeishan large igneous province. Int. Geol. Rev. 45, 753–766.
Xiao, L., Xu, Y.G., Mei, H.J., Zheng, Y.F., He, B., Pirajno, F., 2004. Distinct mantle sources of low-Ti and high-Ti basalts from the western Emeishan large igneous province, SW China: implications for plume–lithosphere interaction. Earth Planet. Sci. Lett. 228, 525–546.
Xu, Y.G., He, B., 2007. Thick and high velocity crust in Emeishan large igneous province, SW China: evidence for crustal growth by magmatic underplating/intraplating. In: Foulger, G., Jurdy, D. (Eds.), The Origins of Melting Anomalies: Plates, Plumes, and Planetary Processes. Geological Society of America Special Publication, 430, pp. 841–858.
Xu, Y.-G., Chung, S.-L., Jahn, B.-M., Wu, G., 2001. Petrologic and geochemical constraints on the petrogenesis of Permian–Triassic Emeishan flood basalts in southwestern China. Lithos 58, 145–168.
Xu, Y.-G., He, B., Chung, S.-L., Menzies, M.A., Frey, F.A., 2004. Geologic, geochemical, and geophysical consequences of plume involvement in the Emeishan flood–basalt province. Geology 32, 917–920.
Xu, Y.-G., Luo, Z.-Y., Huang, X.-L., He, B., Xiao, L., Xie, L.-W., Shi, Y.-R., 2008. Zircon U–Pb and Hf isotope constraints on crustal melting associated with the Emeishan mantle plume. Geochim. Cosmochim. Acta 72, 3084–3104.
Xu, Y.-G., Chung, S.-L., Shao, H., He, B., 2010. Silicic magmas from the Emeishan large igneous province, Southwest China: petrogenesis and their link with the end-Guadalupian biological crisis. Lithos 119, 47–60.
Yaxley, G.M., Green, D.H., 1998. Reactions between eclogite and peridotite: mantle refertilisation by subduction of oceanic crust. Schweiz. Mineral. Petrogr. Mitt. 78, 243–255.
Yunnan, 1990. Regional geology of Yunnan province. Geological Memoirs, Series, 21. Geologic Press, Beijing (in Chinese).
Zhang, H.F., Sun, M., Lu, F.X., Zhou, X.H., Zhou, M.F., Liu, Y.S., Zhang, G.H., 2001. Moderately depleted lithospheric mantle underneath the Yangtze Block: evidence from a garnet lherzolite xenolith in the Dahongshan kimberlite. Geochem. J. 35, 315–331.
Zhang, Z.-C., Mao, J.-W., Saunders, A.D., Ai, Y., Li, Y., Zhao, L., 2009. Petrogenetic modeling of three mafic–ultramafic layered intrusions in the Emeishan large igneous province, SW China, based on isotopic and bulk chemical constraints. Lithos 113, 369–392.
Zhang, X.-Q., Song, X.-Y., Chen, L.-M., Xie, W., Yu, S.-Y., Zheng, W.-Q., Deng, Y.-F., Zhang, J.-F., Gui, S.-G., 2012. Fractional crystallization and the formation of thick Fe–Ti–V oxide layers in the Baima layered intrusion SW China. Ore Geol. Rev. 49, 96–108.
Zhao, J.H., Zhou, M.F., Yan, D.P., Yang, Y.H., Sun, M., 2008. Zircon Lu–Hf isotopic constraints on Neoproterozoic subduction-related crustal growth along the western margin of the Yangtze Block South China. Precambrian Res. 163, 189–209.
Zhong, H., Zhu, W.-G., 2006. Geochronology of layered mafic intrusions from the Pan–Xi area in the Emeishan large igneous province, SW China. Miner. Depos. 41, 599–606.
Zhong, H., Zhou, X.-H., Zhou, M.-F., Sun, M., Liu, B.-G., 2002. Platinum-group element geochemistry of the Hongge Fe–V–Ti deposit in the Pan–Xi area, southwestern China. Miner. Depos. 37, 226–239.
Zhong, H., Yao, Y., Hu, S., Zhou, X., Liu, B., Sun, M., Zhou, M., Viljoen, M., 2003. Trace-element and Sr–Nd isotopic geochemistry of the PGE-bearing Hongge layered intrusion, Southwestern China. Int. Geol. Rev. 45, 371–382.
Zhong, H., Yao, Y., Prevec, S.A., Wilson, A.H., Viljoen, M.J., Viljoen, R.P., Liu, B.-G., Luo, Y.-N., 2004. Trace-element and Sr–Nd isotopic geochemistry of the PGE-bearing Xinjie layered intrusion in SW China. Chem. Geol. 203, 237–252.
Zhong, H., Zhu, W.-G., Chu, Z.-Y., He, D.-F., Song, X.-Y., 2007. Shrimp U–Pb zircon geochronology, geochemistry, and Nd–Sr isotopic study of contrasting granites in the Emeishan large igneous province, SW China. Chem. Geol. 236, 112–133.
Zhong, H., Zhu, W.-G., Hu, R.-Z., Xie, L.-W., He, D.-F., Liu, F., Chu, Z.-Y., 2009. Zircon U–Pb age and Sr–Nd–Hf isotope geochemistry of the Panzhihua A-type syenitic intrusion in the Emeishan large igneous province, southwest China and implications for growth of juvenile crust. Lithos 110, 109–128.
Zhong, H., Qi, L., Hu, R.-Z., Zhou, M.-F., Gou, T.-Z., Zhu, W.-G., Liu, B.-G., Chu, Z.-Y., 2011. Rhenium–osmium isotope and platinum-group elements in the Xinjie layered intrusion, SW China: implications for source mantle composition, mantle evolution, PGE fractionation and mineralization. Geochim. Cosmochim. Acta 75, 1621–1641.
Zhou, M.-F., Malpas, J., Song, X.-Y., Robinson, P.T., Sun, M., Kennedy, A.K., Lesher, C.M., Keays, R.R., 2002a. A temporal link between the Emeishan large igneous province (SW China) and the end-Guadalupian mass extinction. Earth Planet. Sci. Lett. 196, 113–122.
Zhou, M.-F., Yan, D.-P., Kennedy, A.K., Li, Y., Ding, J., 2002b. SHRIMP U–Pb zircon geochronological and geochemical evidence for Neoproterozoic arc-magmatism along the western margin of the Yangtze Block South China. Earth Planet. Sci. Lett. 196, 51–67.
Zhou, M.-F., Yang, Z.X., Song, X.Y., Keays, R.R., Lesher, C.M., 2002c. Magmatic Ni–Cu–(PGE) sulfide deposits in China. In: Cabri, L.J. (Ed.), The Geology, Geochemistry, Mineralogy, Mineral Beneficiation of the Platinum-Group Elements. Canadian Institute of Mining, Metallurgy and Petroleum, Special Volume, 54, pp. 619–636.
Zhou, M.-F., Robinson, P.T., Lesher, C.M., Keays, R.R., Zhang, C.-J., Malpas, J., 2005. Geochemistry, petrogenesis and metallogenesis of the Panzhihua gabbroic layered intrusion and associated Fe–Ti–V oxide deposits, Sichuan Province, SW China. J. Petrol. 46, 2253–2280.
Zhou, M.-F., Arndt, N.T., Malpas, J., Wang, C.Y., Kennedy, A.K., 2008. Two magma series and associated ore deposit types in the Permian Emeishan large igneous province, SW China. Lithos 103, 352–368.